exhibit a liver condition similar to human NASH, which is associated with obesity, insulin resistance, and dyslipidemia [13]. They also develop well-differentiated hepatocellular carcinoma after a longer period of time [13]. Moreover, they show enhanced adipose tissue inflammation characterized by macrophage infiltration and adipocytokine dysregulation [13], which may contribute to excessive lipid accumulation and enhanced fibrosis in the liver [14,15,16,17,18]. MC4R is a seven-transmembrane G protein-coupled receptor that is expressed in the hypothalamic nuclei implicated in the regulation of food intake and body weight [19]. Because MC4R mRNA expression is restricted to the hypothalamus and other brain regions and is undetectable in the liver and the adipose tissue [20], it is likely that the hepatic phenotype in MC4R-KO mice results from loss of function of MC4R in the brain rather than in the liver itself. In line with this, Nogueiras *et al.* reported that MC4R signaling in the brain may regulate lipid metabolism in the liver [21]. Collectively, MC4R-KO mice would provide a novel mouse model of NASH with which to investigate the sequence of events that comprise diet-induced steatosis and fibrosis in the liver.

Evidence has accumulated indicating that obesity is a state of chronic, low-grade inflammation, which may play a role in the pathogenesis of obesity-related complications [22]. There is also considerable evidence that macrophages are infiltrated into obese adipose tissue to induce inflammatory responses [22,23,24]. Recent studies have pointed to the heterogeneity of macrophages in obesity; *i.e.* M1 or "classically activated" (proinflammatory) macrophages and M2 or "alternatively activated" (anti-inflammatory) macrophages [25,26]. Adipose tissue macrophages in lean mice are polarized toward the M2 activation state, whereas in obese adipose tissue, they are toward the M1 activation state [25]. Histologically, M2 macrophages are scattered in the interstitial spaces between adipocytes [26]. On the other hand, CD11c-positive M1 macrophages aggregate to constitute crown-like structures (CLS) in obese adipose tissue of humans and rodents, where they are considered to scavenge the residual lipid droplets of dead adipocytes [27]. Notably, the number of CLS is positively correlated with systemic hyperinsulinemia and insulin resistance in obese subjects [28,29], suggesting the pathophysiologic role of CLS in adipose tissue inflammation.

Here we report that CD11c-positive macrophages aggregate to constitute CLS-like structures surrounding hepatocytes with large lipid droplets in the liver from MC4R-KO mice fed a Western diet (WD), which may be referred to as "hepatic CLS (hCLS)". Notably, the number of hCLS is positively correlated with the extent of liver fibrosis in our NASH model. We also observed increased number of hCLS in the liver of NAFLD/NASH patients, whereas it is rarely detected in patients with chronic viral hepatatis. Collectively, our data provide evidence that hCLS is critically involved in the development of hepatic inflammation and fibrosis, thereby suggesting its pathophysiologic role in disease progression from simple steatosis to NASH.

Materials and Methods

Ethics Statement

All animal experiments were conducted in accordance to the guidelines of Tokyo Medical and Dental University Committee on Animal Research (No. 2011-207C, No. 0130269A). The clinical study protocol was approved by the ethical committee on human research of Tokyo Medical and Dental University, Yamaguchi University Hospital, and Heart Life Hospital (No. 1366 and No. 1397, Medical Research Ethics Committee of Tokyo Medical and Dental University; H24–80, Institutional Review Board of Yamaguchi University Hospital; 24-6, Institutional Review Board of Heart Life Hospital). The study is a follow-back study using only existing materials and information including human biological specimens. All samples were collected and stored for clinical practice at Yamaguchi University Hospital and Heart Life Hospital. Although written informed consent was not obtained for the current study, we obtained approval from Ethics Committee/Institutional Review Board of each institution based on Japanese Ethical Guidelines for Clinical Studies, disclosed the detailed information on the study protocol, and provided all participants with an opportunity to refuse their inclusion in the study.

Animals

The MC4R-KO mice on the C57BL/6J background were a generous gift from Dr. Joel K. Elmquist (University of Texas Southwestern Medical Center) [19]. Male C57BL/6J wildtype mice were purchased from CLEA Japan (Tokyo, Japan). The animals were acclimated to the environment in a temperature-, humidity-, and light-controlled room (12-h light and 12-h dark cycle) and allowed free access to water and a standard chow (CE-2; 343.1 kcal/100 g, 12.6% energy as fat; CLEA Japan) for one week. Eight week-old male mice were fed a WD (D12079B; 468 kcal/100 g, 41% energy as fat, 34.0% sucrose, 0.21% cholesterol; Research Diets, New Brunswick, NJ) or a HFD (D12492; 524 kcal/100 g, 60% energy as fat, 8.9% sucrose, 0.03% cholesterol; Research Diets). Methionine and choline-deficient diet (#518810; Dyets, Bethlehem, PA) was used to induce steatohepatitis. At the end of the experiment, they were sacrificed, when fed *ad libitum*, under intraperitoneal pentobarbital anesthesia (30 mg/kg).

Blood Analysis

Blood glucose concentrations and serum concentrations of alanine aminotransferase (ALT), total cholesterol (TC), triglyceride (TG), free fatty acid, and insulin were measured as previously described [13].

Hepatic TC and TG Content

Total lipids in the liver were extracted with ice-cold 2:1 (vol/vol) chloroform/methanol. The TC and TG concentrations were measured by an enzymatic assay kit (Wako Pure Chemicals, Osaka, Japan) [13].

Histological Analysis

The liver was fixed with neutral-buffered formalin and embedded in paraffin. Four-μm-thick sections of the liver were stained with Masson-trichrome and Sirius red [13]. Immunohistochemical staining for F4/80, α-smooth muscle actin (αSMA) (ab5694, Abcam, Cambridge, UK), and type I collagen (1310-01, Southern Biotech, Birmingham, AL) were performed [30]. Positive areas for Sirius red, αSMA, and F4/80 were measured using the software WinROOF (Mitani, Chiba, Japan) [13]. The number of hCLS was counted in the whole area of each F4/80-stained section and expressed as the mean number/mm^2. For immunofluorescent staining, the liver was embedded in OCT compound and frozen in dry ice-acetone. Ten-μm-thick frozen sections were stained with antibodies against F4/80, type I collagen, fibroblast specific protein 1 (FSP1) (ab27957, Abcam), glial fibrillary acidic protein (GFAP) (Z0334, Dako, Glostrup, Denmark), CD11c (14-0114, eBioscience, San Diego, CA), and secondary antibodies conjugated with AlexaFluor 488, 568 or 594 (Invitrogen, Carlsbad, CA) and Alexa Fluor 647 (Jackson ImmunoResearch

Labolatories, West Grove, PA). Lipid droplets were defined by BODIPY 493/503 (Invitrogen). Sections were mounted in Vectashield mounting medium with DAPI (VectorLabs, Burlingame, CA) and photographed using confocal laser-scanning microscope FV10i-DOC (Olympus, Tokyo, Japan).

Electron Microscopy

Liver samples were fixed in 2.5% glutaralehyde in 0.1 M cacodylate buffer for 1 hour, and postfixed in 1% osmium tetroxide. After dehydration in a graded series of ethanol solutions and propylene oxide and embedding in Epon 812, ultrathin sections were cut by use of an Ultratome, stained with uranyl acetate and lead citrate, and observed with a Hitachi H-7500 electron microscope (Hitachi, Tokyo, Japan).

Macrophage depletion experiment with clodronate liposomes

Clodronate liposomes were prepared as described previously [31]. In brief, phosphatidylcholine from egg (Avanti Polar Lipids, Alabaster, AL) and cholesterol (Wako Pure Chemicals, Osaka, Japan) were dissolved in chloroform in a glass tube, followed by evaporation of chloroform using nitrogen gas, resulting in a thin layer film. The tube containing the film was dried in a desiccator overnight. Clodronate disodium (Sigma, St. Louis, MO) dissolved in phosphate-buffered saline (PBS) was added to the tube containing the film, and then liposomes were generated by vortexing. The liposome-containing solution was frozen and thawed three times, and subsequently passed through an extruder (Avanti) with a 400 nm membrane. After centrifugation at 10,000× g for 15 minutes, clodronate liposomes were suspended in sterilized PBS. To deplete macrophages, MC4R-KO and wildtype mice fed a WD for 4 or 20 weeks received 0.1 ml of clodronate or PBS liposomes via the tail vein at 6 and 2 days before the end of the experiment.

Quantitative Real-Time PCR

Total RNA was extracted from the liver using Sepasol reagent (Nacalai Tesque, Kyoto, Japan). Quantitative real-time PCR was performed with StepOnePlus Real-time PCR System using Fast SYBR Green Master Mix Reagent (Applied Biosystems, Foster City, CA) as described previously [32]. Primers used in this study were described elsewhere [13].

Human Study

Fifty-one Japanese NAFLD patients who had sustained liver dysfunction and 15 chronic viral hepatitis patients were recruited at Yamaguchi University hospital and Heart Life Hospital. We measured body mass index (BMI), and determined plasma concentrations of aspartate aminotransferase (AST) and ALT according to the standard procedures. Liver samples were obtained by ultrasound-guided liver biopsy to evaluate liver histology [33]. Formalin-fixed and paraffin embedded liver specimens were stained with anti-CD68 antibody (M0876, Dako). The liver histology was assessed by two investigators without knowledge of the origin of the slides according to the NASH clinical research network scoring system, including the scores for hepatic steatosis, lobular inflammation, ballooning degeneration and the fibrosis stage [34]. The number of hCLS was counted in the whole area of each CD68-stained section and expressed as the mean number/mm^2.

Statistical Analysis

Data are presented as mean ± SE, and $P<0.05$ was considered statistically significant. Differences between two groups were compared using Student *t*-test. Pearson correlation coefficient was employed to investigate the correlation among hCLS number, F4/80-positive area, and fibrosis area. Tests for linear trend were calculated by assigning the average numbers of hCLS for each score of hepatic steatosis, lobular inflammation, ballooning degeneration, and fibrosis stage treated as a continuous variable by using linear regression models. All data were analyzed with Stat View version 5.0 or JMP version 10.0 (SAS Institute Inc, Cary, NC).

Results

Hepatic phenotypes of MC4R-KO mice

The MC4R-KO mice showed marked increase in body weight and liver weight relative to wildtype mice after 20-week WD feeding (Figure 1A and 1B). They also exhibited increased concentrations of insulin, TC, and ALT and hepatic accumulation of TC as well as TG (Table 1). At this time point, microvesicular steatosis was observed uniformly in the liver from wildtype mice, where inflammatory cell infiltration and tissue fibrosis were rarely observed (Figure 1C). On the other hand, livers from MC4R-KO mice fed a WD exhibited micro- and macrovesicular steatosis, ballooning degeneration, massive infiltration of inflammatory cells, and marked pericellular fibrosis (Figure 1C) as we previously reported using a HFD [13]. Although the area of liver fibrosis was not increased in wildtype mice throughout the experimental period, MC4R-KO mice developed obvious liver fibrosis at 20 weeks of WD feeding ($P<0.01$, Figure 1D). Moreover, the area of αSMA-positive activated fibroblasts was significantly increased in MC4R-KO mice relative to wildtype mice at 8 and 20 weeks (Figure 1E) [13]. We next examined the distribution of macrophages in the liver with F4/80 immunostaining, a representative macrophage marker. In wildtype mice fed a WD, macrophages showed scattered distribution in the liver (Figure 1F). On the other hand, in MC4R-KO mice fed a WD, macrophages aggregated to surround hepatocytes with large lipid droplets (Figure 1F). Given the structural similarity to CLS in obese adipose tissue, it may be referred to as "hepatic CLS". Although the area positive for F4/80 immunostaining was roughly comparable between the genotypes throughout the experimental period (Figure 1G), the number of hCLS was significantly increased in MC4R-KO mice relative to wildtype mice at 4 weeks, when liver fibrosis was not evident, and thereafter increased time-dependently up to 20 weeks (Figure 1H). Notably, after 20-week WD, the number of hCLS, not the F4/80-positive area, was positively correlated with the extent of liver fibrosis (Figure 1I and 1J).

We confirmed the results in MC4R-KO mice fed a HFD for 20 weeks (Figure S1A-S1C). hCLS was also observed in the liver from wildtype mice fed a HFD for one year, at which they develop liver fibrosis comparable to MC4R-KO mice on a HFD for 20 weeks (Figure S1D and S1E). Furthermore, hCLS was also present in mice fed a methionine and choline-deficient diet, a well-known model of steatohepatitis (Figure S1F and S1G). Collectively, these observations suggest that hCLS is a common histological feature in steatohepatitis models, which precedes the development of collagen deposition and reflects the extent of liver fibrosis.

Histological characterization of hCLS in MC4R-KO mice

To investigate the histological characteristics of hCLS, we performed immunohistochemical analysis using the liver from wildtype and MC4R-KO mice fed a WD for 20 weeks. The serial liver sections stained with antibodies against F4/80, αSMA, and type I collagen revealed that αSMA-positive myofibroblasts and collagen deposition are located in proximity to hCLS in the liver

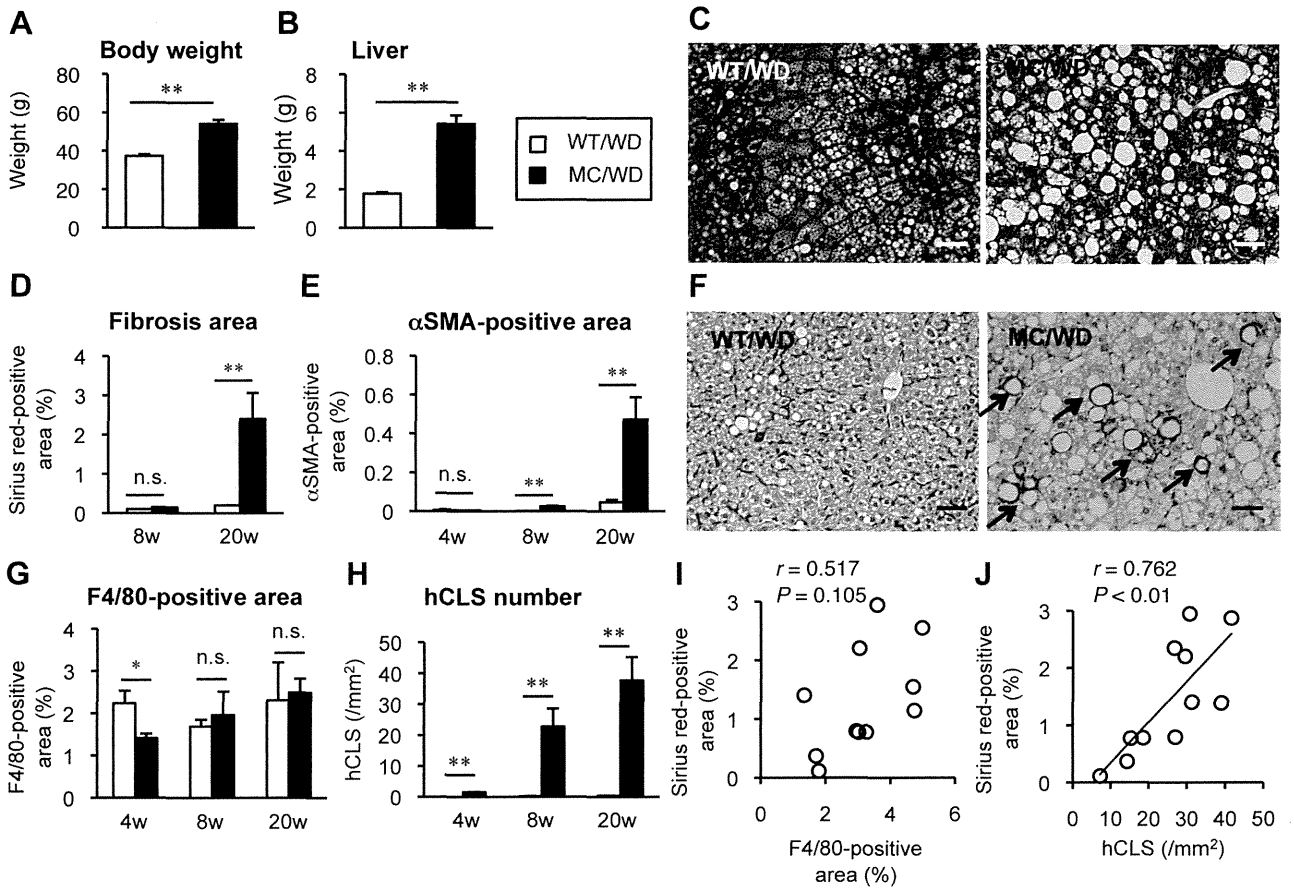

Figure 1. hCLS formation by macrophages and liver fibrosis in MC4R-KO mice fed a WD. Body weight (A) and liver weight (B) of male MC4R-KO (MC) and wildtype (WT) mice fed a western diet (WD) for 20 weeks. (C) Masson-trichrome staining of the liver sections from MC4R-KO and wildtype mice after 20 weeks of WD feeding. Time-dependent changes in liver fibrosis (Sirius red-positive area) (D) and activated fibroblasts (αSMA-positive area) (E) during WD feeding. (F) F4/80 staining at 20 weeks. Characteristic histological features by macrophage, hepatic crown-like structures (hCLS), in the liver from MC4R-KO mice were indicated by arrows. Time-dependent changes in F4/80-positive area (G) and hCLS number (H) during WD feeding. Correlation of fibrosis area with F4/80-positive area (I) and hCLS number (J). Scale bars, 50 μm. * $P<0.05$, ** $P<0.01$, n.s., not significant. $n=5$–7.
doi:10.1371/journal.pone.0082163.g001

Table 1. Serological parameters and hepatic lipid content of MC4R-KO and WT mice fed a WD for 20 weeks.

	WT		MC4R-KO	
	SD	WD	SD	WD
BG (*ad lib*, mg/dL)	147.7±0.8	195.3±7.2*	156.6±16.8	151.4±7.1§
Insulin (*ad lib*, ng/mL)	0.47±0.15	1.10±0.11	3.41±1.16	4.72±1.84*
TC (mg/dL)	93.7±4.4	204.3±8.7*	130.2±11.2	352.1±35.1*§†
TG (mg/dL)	112.5±18.2	48.9±3.7*	146.3±25.5	69.9±10.1†
FFA (mEq/L)	0.38±0.04	0.32±0.01	0.61±0.06*	0.52±0.03*§
ALT (IU/L)	30.0±1.4	43.4±10.9	56.8±18.7	268.7±34.8*§†
Liver TC (mg/g tissue)	1.88±0.46	1.64±0.24	2.58±0.46	4.83±1.14*§
Liver TG (mg/g tissue)	37.9±8.3	54.5±6.9	61.0±10.4	133.6±35.8*

WT, wildtype; SD, standard diet; WD, western diet; BG, blood glucose; TC, total cholesterol; TG, triglyceride; FFA, free fatty acid; ALT, alanine aminotransferase. Data are expressed as the mean ± SE. *$P<0.05$ vs. WT-SD; §$P<0.05$ vs. WT-WD; †$P<0.05$ vs. MC4R-SD. $n=5$-7.
doi:10.1371/journal.pone.0082163.t001

from MC4R-KO mice (Figure 2A). There were no apparent collagen deposition in the liver from wildtype mice (data not shown). By double-immunofluorescent staining of F4/80 (green) and type I collagen (red), we also observed the adjacent spatial relationship between hCLS and fibrogenic lesions (Figure 2B and 2E). Since previous reports pointed to the heterogeneity of fibrogenic cells during the development of liver fibrosis [35,36,37], we examined the expression of GFAP and FSP1, markers for hepatic stellate cells and fibroblasts, respectively. The GFAP-positive cells were diffusely located along the sinusoids in wildtype and MC4R-KO mice (Figure 2C and 2F). The FSP1-positive cells accumulated around hCLS in MC4R-KO mice, whereas they were only sparsely observed in wildtype mice (Figure 2D and 2G). Notably, CD11c was positive only in macrophages that constitute hCLS (Figure 2H). In this study, BODIPY staining revealed that hepatocytes surrounded by hCLS have large lipid droplets (Figure 2I). In electron microscopic analysis, some macrophages having cell processes on the surface and lysosomes in the cytoplasm, assembled around lipid droplets to form hCLS (Figure 2J). Taken together, our data suggest that hCLS is associated with fibrogenic lesions in the liver from MC4R-KO mice on a WD.

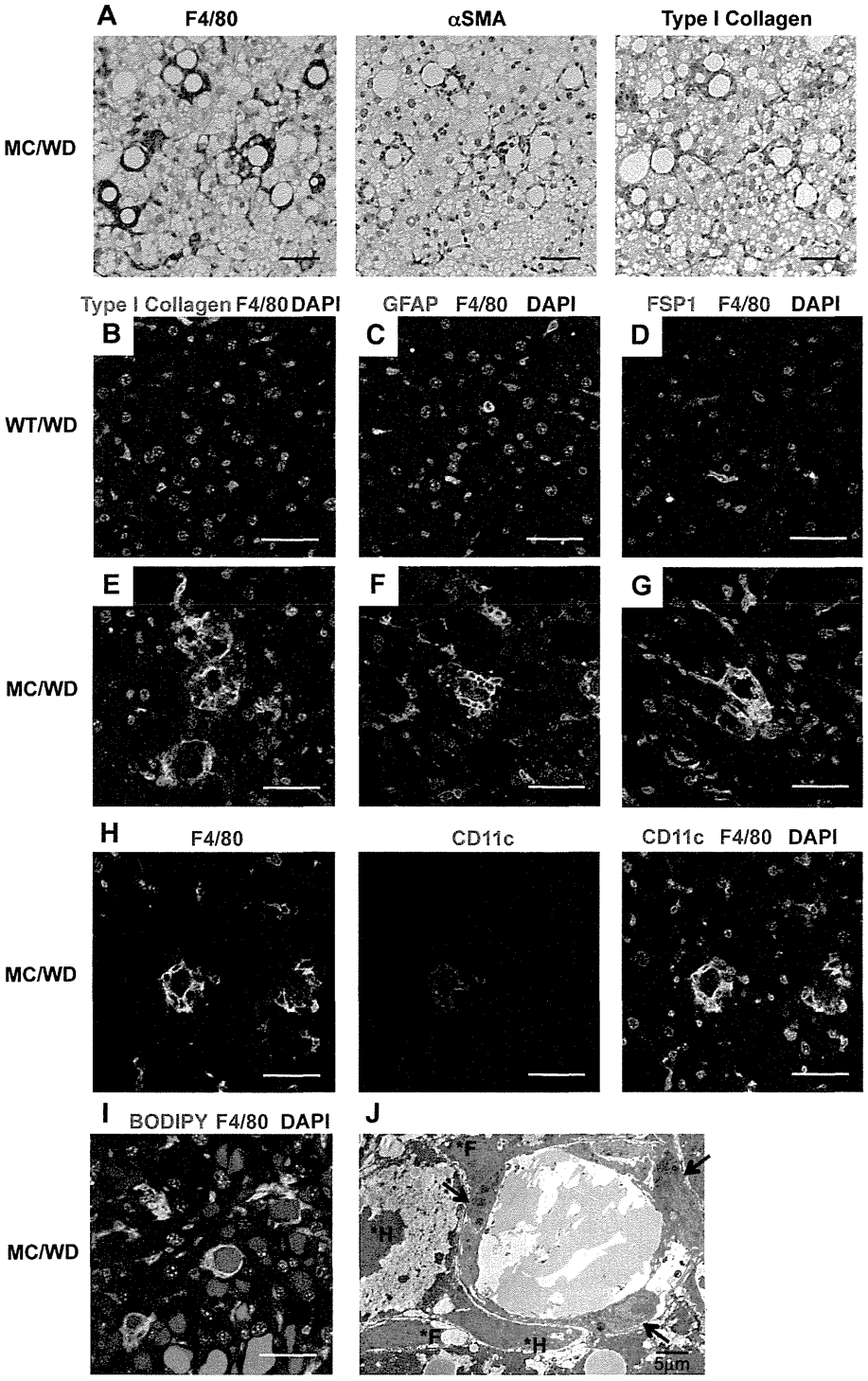

Figure 2. Histological analysis of hCLS in the liver from MC4R-KO mice fed a WD. (A) Serial sections of the liver from MC4R-KO mice fed a WD for 20 weeks stained with F4/80, αSMA, and type I collagen antibodies. Immunofluorescent analysis for F4/80 (B-G), type I collagen (B, E), glial fibrillary acidic protein (GFAP) (C, F), and fibroblast specific protein 1 (FSP1) (D, G) in the liver from wildtype and MC4R-KO mice at 20 weeks. (H) Immunofluorescent analysis for F4/80 and CD11c. (I) Immunofluorescent analysis for F4/80 and lipid droplet (BODIPY). The nuclei were counterstained with DAPI (B–I). Scale bars, 50 μm. (J) Electron micrograph of hCLS. Aggregated macrophages around a lipid droplet (arrows). Fibroblasts (*F) and hepatocytes (*H) are detected around hCLS.
doi:10.1371/journal.pone.0082163.g002

Effect of clodronate liposomes on inflammation and fibrosis in MC4R-KO mice

We next examined the functional role of hCLS in hepatic inflammation and fibrosis in MC4R-KO mice on a WD. Administration of clodronate liposomes effectively depleted F4/80-positive macrophages in the steatotic liver from wildtype mice fed a WD for 20 weeks (Figure 3A). Expression of mRNAs for inflammatory genes (F4/80 and TNFα) and fibrogenic genes (transforming growth factor-β1 and tissue inhibitor of metalloproteinase-1) was significantly reduced by treatment with clodronate liposomes (Figure 3B). We also confirmed similar results in the liver from MC4R-KO mice fed a WD for 4 weeks, when they showed simple hepatic steatosis (Figure 3C and 3D). In MC4R-KO mice fed a WD for 20 weeks, macrophages showing scattered distribution in the liver were also depleted by the treatment (Figure 3E). However, macrophages constituting hCLS were resistant to the treatment with clodronate liposomes (Figure 3E). In this setting, treatment with clodronate liposomes resulted in no significant changes in mRNA expression of TNFα and fibrogenic genes (Figure 3F). We confirmed that F4/80-positive area was significantly decreased by the treatment with clodronate liposomes, whereas the number of hCLS and the αSMA-positive area were unchanged (Figure 3G–3I). These observations suggest that hCLS is an important source of hepatic inflammatory and fibrogenic mediators in MC4R-KO mice on a WD.

hCLS in human NASH

To elucidate the clinical implications of hCLS, we next performed macrophage immunostaining using liver biopsy specimens from patients with NAFLD/NASH and chronic viral hepatitis caused by hepatitis B and C viruses. There were no significant differences in age and plasma AST and ALT concentrations between the patients. Body mass index was significantly higher in patients with NAFLD/NASH relative to those with chronic viral hepatitis (Table 2). CD68 immunostaining revealed macrophage aggregation constituting hCLS in the liver from NAFLD/NASH patients (Figure 4A, 4B, and 4D), which was rarely observed in patients with chronic viral hepatitis (Figure 4C and 4D). We further examined the correlation of the number of hCLS with the scores for hepatic steatosis, lobular inflammation, ballooning degeneration and the fibrosis stage in patients with NAFLD/NASH (Figure 4E–4H). The number of hCLS tended to be high in the patients with massive hepatic steatosis, which did not reach a statistical significance (Figure 4E) and there was a negative trend between the number of hCLS and the score for lobular inflammation (Figure 4F). Interestingly, the number of hCLS was positively associated with the score for ballooning degeneration, which is a hallmark for hepatocyte injury (Figure 4G). The patients with fibrosis stage 2 showed the highest number of hCLS (Figure 4H), which is consistent with our observations that most of the MC4R-KO mice fed a WD for 20 weeks exhibited liver fibrosis corresponding to fibrosis stage 2 in the scoring system for human NASH. These observations indicate that human NAFLD/NASH also exhibits hCLS formation, which may be associated with hepatocyte injury.

Discussion

NASH is a severe form of NAFLD, and can progress to cirrhosis and hepatocellular carcinoma. However, it is currently unclear how simple hepatic steatosis progresses to NASH. Since macrophages play a variety of roles during the process of inflammation such as production of proinflammatory cytokines and chemokines, recruitment of immune cells, phagocytosis of dead cells, and production and degradation of extracellular matrices, macrophages should be involved in the pathogenesis of NASH. In this study, using a novel mouse model of NASH that reflects a liver condition of human NASH, we observed that macrophages aggregate to constitute hCLS surrounding hepatocytes with large lipid droplets. We have also demonstrated for the first time that the number of hCLS is positively correlated with the extent of liver fibrosis. In this regard, it is noteworthy that hCLS is clearly observed in the liver of patients with NAFLD/NASH. hCLS was also observed in other experimental models of steatohepatitis induced by a long term-HFD feeding or methionine choline-deficient diet. These observations suggest that hCLS would be a common histological feature for steatohepatitis.

Since hepatic macrophages exacerbate steatosis and lipid-mediated injuries in the liver [38,39], it is important to know how macrophages contribute to the pathogenesis of NASH. Evidence has accumulated suggesting that macrophages play an important role in liver fibrosis *in vivo*. For instance, Kupffer cell inactivation or macrophage depletion results in lower scarring and reduced activation of hepatic stellate cells in the carbon tetrachloride-induced liver fibrosis [10,33,40]. In contrast, macrophage depletion at the onset of fibrosis resolution retards extracellular matrix degradation [10]. Infusion of autologous bone marrow cells including macrophages are clinically effective to repair and regenerate liver cirrhosis [41,42]. All the reports point to the functionally distinct subpopulations of macrophages in the liver during the progression and recovery of liver fibrosis. Studies with clodronate liposomes suggest that macrophages in hCLS express inflammatory and fibrogenic genes at higher levels than those scattered in the liver from MC4R-KO mice fed a WD. Histologically, hCLS formation precedes the development of collagen deposition and is located close to fibrogenic lesions. Moreover, the number of hCLS is positively correlated with the extent of liver fibrosis. It is, therefore, conceivable that hCLS promotes liver fibrosis, which may be involved in the progression from simple steatosis to NASH.

In this study, we show that hCLS-constituting macrophages are positive for CD11c and may engulf dead hepatocytes and residual lipids in their phagosomes. The histological features are reminiscent of CLS in obese adipose tissue, in which CD11c-positive M1 macrophages surround and scavenge dead adipocytes and residual lipids [25,27]. It is also known that ablation of CD11c-positive cells leads to a marked decrease in adipose tissue inflammation and normalizes insulin sensitivity without affecting body weight [43]. However, little is known about the involvement of CD11c-positive macrophages in fibrogenesis. Recent evidence has pointed to the role of intimate crosstalk between parenchymal and interstitial cells in the pathogenesis of chronic inflammatory diseases [14,44]. It is now recognized that endogenous stress signals, which are referred to as "danger signals" released from necrotic cells and damaged tissues, are sensed by the innate immune system, thereby inducing sterile inflammation [14,44]. Thus, the interaction between dying hepatocytes and hCLS-constituting macrophages may be key to understand the molecular mechanisms underlying the development of liver fibrosis in NASH. Interestingly, treatment with clodronate liposomes failed to deplete macrophages in hCLS in MC4R-KO mice on a WD, suggesting the impaired phagocytic function. This is consistent with the super-paramagnetic iron oxide magnetic resonance imaging study showing defective phagocytic function in macrophages in the liver of NASH patients [45]. Further studies are required to understand how macrophages in hCLS affect hepatic stellate cells or fibroblasts to promote fibrosis in the liver.

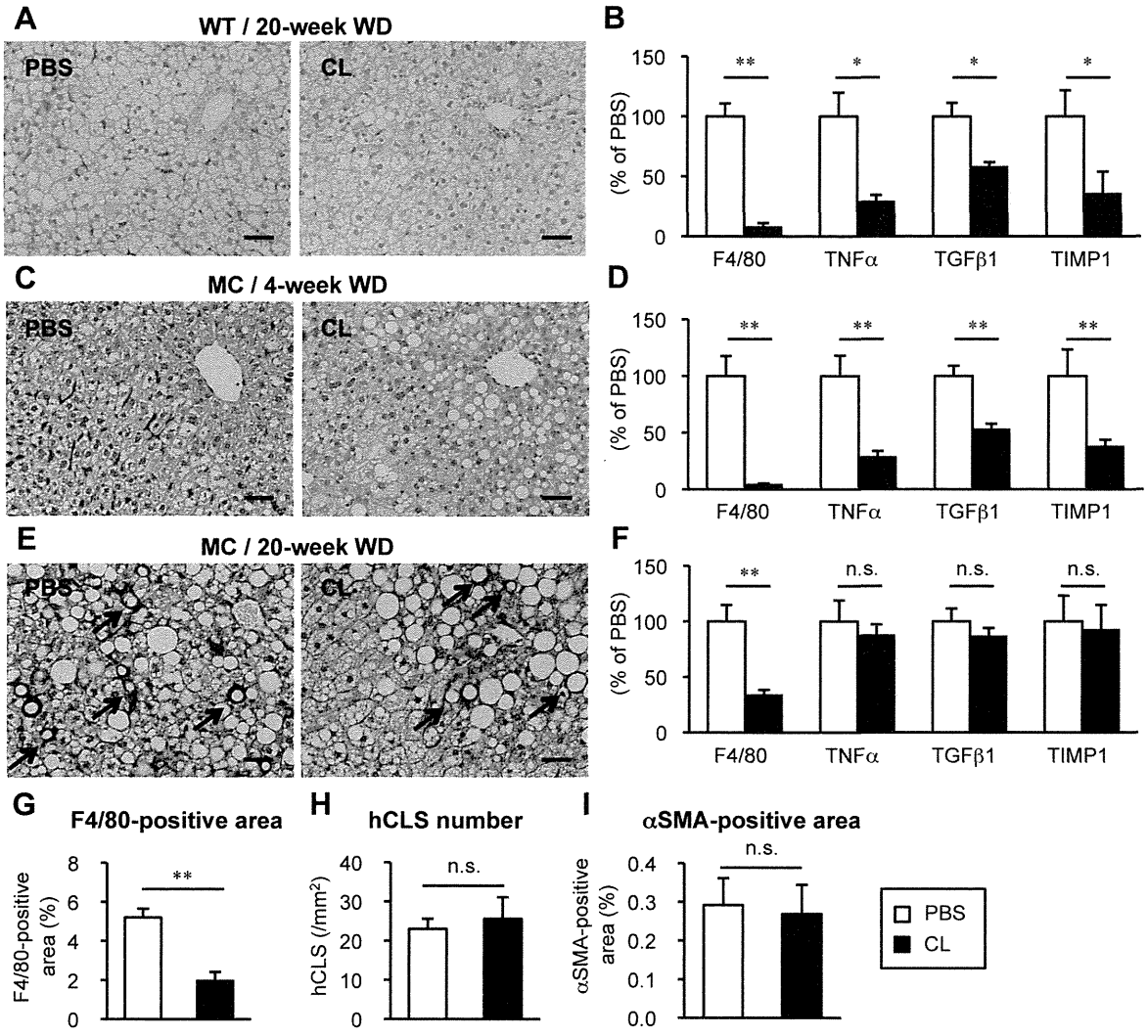

Figure 3. Effect of Macrophage depletion on inflammatory and fibrotic changes in the liver during WD feeding. Representative F4/80 immunostaining (A) and hepatic mRNA expression of inflammatory markers (F4/80, and tumor necrosis factor α (TNFα) and fibrogenic factors (transforming growth factor-β1 (TGFβ1) and tissue inhibitor of metalloproteinase-1 (TIMP1)) (B) in the liver from wildtype mice fed a WD for 20 weeks, at which wildtype mice showed simple steatosis. Representative F4/80 immunostaining (C, E) and hepatic mRNA expression levels (D, F) in the liver from MC4R-KO mice fed a WD for 4 (C, D) and 20 weeks (E, F), at which MC4R-KO mice showed simple steatosis and NASH respectively. Arrows indicate hCLS. Quantification of F4/80-positive area (G), hCLS number (H) and αSMA-positive area (I) at 20 weeks. PBS, PBS liposome; CL, clodronate liposome. Scale bars, 50 μm. * $P<0.05$, ** $P<0.01$, n.s., not significant. $n=5–7$.
doi:10.1371/journal.pone.0082163.g003

In this study, we demonstrate that hCLS is observed in patients with NAFLD/NASH. Interestingly, there was a positive association between the number of hCLS and the score for ballooning degeneration, which is consistent with our histological data in MC4R-KO mice that macrophages constituting hCLS may scavenge the residual lipid droplets of dead hepatocytes. On the other hand, the number of hCLS was not positively associated with the scores for hepatic steatosis and lobular inflammation. These findings support the notion that hCLS is related to the local inflammation around dying hepatocytes. In this regard, recent evidence has also pointed to the existence of hCLS in human NASH. Rensen *et al.* showed that myeloperoxidase-positive Kupffer cells and neutrophils surround steatotic hepatocytes to constitute hCLS in human NASH [46]. Ioannou *et al.* also showed that CD68-positive macrophages form hCLS around lipid droplets containing cholesterol crystals in human NASH, which was not observed in patients with simple hepatic steatosis [47]. As the degrees of steatosis were not equivalent between NAFLD/NASH and HCV patients in this study, further studies with the full spectrum of patients from simple steatosis to NASH, and/or HCV patients with steatosis are required to elucidate whether hCLS is specific for NAFLD/NASH. Given that hCLS formation precedes the development of collagen deposition in MC4R-KO mice, hCLS could be a prognostic marker for NAFLD/NASH. Since our clinical study is the cross-sectional evaluation of hCLS in patients with NAFLD/NASH, it is interesting to perform a prospective follow-up study to investigate the possibility that hCLS predicts disease progression from simple steatosis to NASH.

Clusters of macrophages have been reported as microgranulomas in human NAFLD/NASH, and those with lipid droplets are referred to as lipogranulomas [48,49]. Lipogranulomas are characterized by a lipid droplet surrounded by macrophages and occasionally eosinophils, lymphocytes, and neutrophils [46,48,50], which may share morphological characteristics with hCLS in this

Table 2. Clinical data of patients with NAFLD/NASH and chronic viral hepatitis.

	NAFLD/NASH	Chronic viral hepatitis
Age	51.2±2.0	56.7±2.8
Sex (male/female)	18/33	9/6
BMI	29.1±0.7	23.3±0.9**
AST (IU/L)	78.7±6.9	53.3±9.4
ALT (IU/L)	122.7±11.5	82.5±20.3

NAFLD, non-alcoholic fatty liver disease; NASH, non-alcoholic steatohepatitis; BMI, body mass index; AST, aspartate aminotransferase; ALT, alanine aminotransferase. Data are expressed as the mean ± SE. **$P<0.01$.
doi:10.1371/journal.pone.0082163.t002

study. To the best of our knowledge, this is the first report to elucidate the potential role of hCLS in liver fibrosis in NASH. In our mouse model, the number of microgranulomas was quite low ($0.18\pm0.03/mm^2$) relative to that of hCLS ($25.61\pm0.18/mm^2$) (M. Itoh *et al.* unpublished observations). It is, therefore, technically difficult to examine the correlation of microgranulomas with the histological scores. On the other hand, the number of microgranuloma in the human biopsies was $3.67\pm0.35/mm^2$, which was much larger than that in MC4R-KO mice. This might be due to the difference in species or the degree of steatosis. In this regard, we do not exclude the possibility that microgranulomas are involved in liver fibrosis in human NASH. In line with this, there are several reports showing the increased number of microgranulomas in NASH relative to simple steatosis and the correlation between the number of microgranulomas and the extent of liver fibrosis [51,52]. Accordingly, it is interesting to know the difference of the role of hCLS and microgranulomas in liver fibrosis.

This study demonstrates for the first time that hCLS is a unique histological feature correlated with liver fibrosis in our mouse model of NASH. We also observed increased number of hCLS in the liver of NAFLD/NASH patients. Our data suggest that in the development of NASH, macrophages constitute hCLS, where they interact with dead hepatocytes and fibrogenic cells, thereby accelerating inflammation and fibrosis in the liver. Collectively, our data provide evidence that hCLS is involved in the development of hepatic inflammation and fibrosis, thereby suggesting its pathophysiologic role in disease progression from simple steatosis to NASH.

Supporting Information

Figure S1 hCLS formation in mouse model of steatohepatitis. Sirius red (A) and F4/80 (B) stainings in the liver of MC4R-KO mice fed a high-fat diet (HFD) for 20 weeks. (C) Correlation of fibrosis area with hCLS number. Sirius red (D) and F4/80 (E) stainings in the liver from wildtype mice fed a HFD for one year. Sirius red (F) and F4/80 (G) stainings in the liver from wildtype mice fed a methionine and choline-deficient diet for 4 weeks. hCLS was indicated by arrows. Scale bars, 50 μm.
(PDF)

Acknowledgments

The authors thank Dr. Joel K. Elmquist (University of Texas Southwestern Medical Center) for the generous gift of MC4R-KO mice and Dr. Jae Bum Kim (Seoul National University) for technical comment on immunohistochemistry. We also thank Ms. Kayoko Sakakibara for technical and secretarial assistances and the members of the Ogawa laboratory for helpful discussions.

Author Contributions

Conceived and designed the experiments: TS YO. Performed the experiments: MI HK KK HS SK MH TF KA. Analyzed the data: MI HK ST YK MT. Wrote the paper: MI HK ST TS YO. Clinical study: YM ST IS. Electron microscopic analysis: YK MT. Statistics: SA.

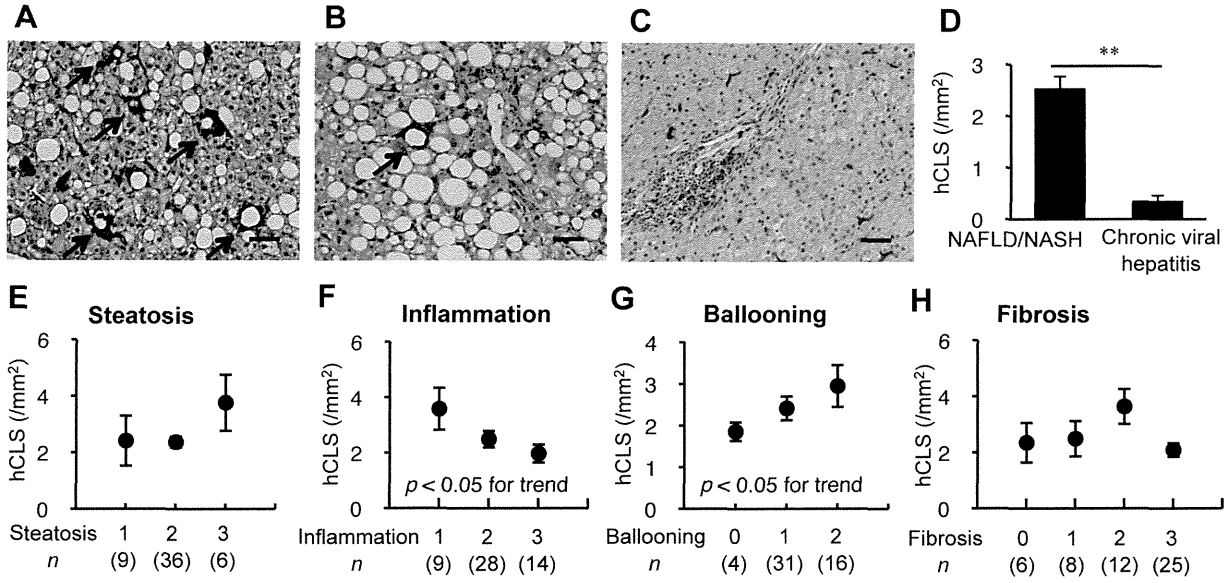

Figure 4. hCLS in human NASH. (A–C) Representative liver sections stained with CD68 antibody in patients with NASH (A), simple hepatic steatosis (B), and chronic viral hepatitis (C). Arrows indicate hCLS. (D) hCLS number in patients with NAFLD/NASH, and chronic viral hepatitis. Correlation of hCLS number with scores for hepatic steatosis (E), lobular inflammation (F), ballooning degenetation (G), and fibrosis stage (H) in patients with NAFLD/NASH. Scale bars, 50 μm. ** $P<0.01$.
doi:10.1371/journal.pone.0082163.g004

References

1. Anstee QM, Targher G, Day CP (2013) Progression of NAFLD to diabetes mellitus, cardiovascular disease or cirrhosis. Nat Rev Gastroenterol Hepatol 10: 330–344.
2. Ratziu V, Bellentani S, Cortez-Pinto H, Day C, Marchesini G (2010) A position statement on NAFLD/NASH based on the EASL 2009 special conference. J Hepatol 53: 372–384.
3. Adams LA, Lymp JF, St Sauver J, Sanderson SO, Lindor KD, et al. (2005) The natural history of nonalcoholic fatty liver disease: a population-based cohort study. Gastroenterology 129: 113–121.
4. Marra F, Gastaldelli A, Svegliati Baroni G, Tell G, Tiribelli C (2008) Molecular basis and mechanisms of progression of non-alcoholic steatohepatitis. Trends Mol Med 14: 72–81.
5. Day CP, James OF (1998) Steatohepatitis: a tale of two "hits"? Gastroenterology 114: 842–845.
6. Browning JD, Horton JD (2004) Molecular mediators of hepatic steatosis and liver injury. J Clin Invest 114: 147–152.
7. Neuschwander-Tetri BA (2010) Hepatic lipotoxicity and the pathogenesis of nonalcoholic steatohepatitis: the central role of nontriglyceride fatty acid metabolites. Hepatology 52: 774–788.
8. Ramadori G, Armbrust T (2001) Cytokines in the liver. Eur J Gastroenterol Hepatol 13: 777–784.
9. Rivera CA, Adegboyega P, van Rooijen N, Tagalicud A, Allman M, et al. (2007) Toll-like receptor-4 signaling and Kupffer cells play pivotal roles in the pathogenesis of non-alcoholic steatohepatitis. J Hepatol 47: 571–579.
10. Duffield JS, Forbes SJ, Constandinou CM, Clay S, Partolina M, et al. (2005) Selective depletion of macrophages reveals distinct, opposing roles during liver injury and repair. J Clin Invest 115: 56–65.
11. Tosello-Trampont AC, Landes SG, Nguyen V, Novobrantseva TI, Hahn YS (2012) Kuppfer cells trigger nonalcoholic steatohepatitis development in diet-induced mouse model through tumor necrosis factor-α production. J Biol Chem 287: 40161–40172.
12. Varela-Rey M, Embade N, Ariz U, Lu SC, Mato JM, et al. (2009) Non-alcoholic steatohepatitis and animal models: understanding the human disease. Int J Biochem Cell Biol 41: 969–976.
13. Itoh M, Suganami T, Nakagawa N, Tanaka M, Yamamoto Y, et al. (2011) Melanocortin 4 receptor-deficient mice as a novel mouse model of nonalcoholic steatohepatitis. Am J Pathol 179: 2454–2463.
14. Suganami T, Tanaka M, Ogawa Y (2012) Adipose tissue inflammation and ectopic lipid accumulation. Endocr J 59: 849–857.
15. Asano T, Watanabe K, Kubota N, Gunji T, Omata M, et al. (2009) Adiponectin knockout mice on high fat diet develop fibrosing steatohepatitis. J Gastroenterol Hepatol 24: 1669–1676.
16. Kamada Y, Tamura S, Kiso S, Matsumoto H, Saji Y, et al. (2003) Enhanced carbon tetrachloride-induced liver fibrosis in mice lacking adiponectin. Gastroenterology 125: 1796–1807.
17. Ikejima K, Takei Y, Honda H, Hirose M, Yoshikawa M, et al. (2002) Leptin receptor-mediated signaling regulates hepatic fibrogenesis and remodeling of extracellular matrix in the rat. Gastroenterology 122: 1399–1410.
18. Imajo K, Fujita K, Yoneda M, Nozaki Y, Ogawa Y, et al. (2012) Hyperresponsivity to low-dose endotoxin during progression to nonalcoholic steatohepatitis is regulated by leptin-mediated signaling. Cell Metab 16: 44–54.
19. Balthasar N, Dalgaard LT, Lee CE, Yu J, Funahashi H, et al. (2005) Divergence of melanocortin pathways in the control of food intake and energy expenditure. Cell 123: 493–505.
20. Gautron L, Lee C, Funahashi H, Friedman J, Lee S, et al. (2010) Melanocortin-4 receptor expression in a vago-vagal circuitry involved in postprandial functions. J Comp Neurol 518: 6–24.
21. Nogueiras R, Wiedmer P, Perez-Tilve D, Veyrat-Durebex C, Keogh JM, et al. (2007) The central melanocortin system directly controls peripheral lipid metabolism. J Clin Invest 117: 3475–3488.
22. Hotamisligil GS (2006) Inflammation and metabolic disorders. Nature 444: 860–867.
23. Berg AH, Scherer PE (2005) Adipose tissue, inflammation, and cardiovascular disease. Circ Res 96: 939–949.
24. Weisberg SP, McCann D, Desai M, Rosenbaum M, Leibel RL, et al. (2003) Obesity is associated with macrophage accumulation in adipose tissue. J Clin Invest 112: 1796–1808.
25. Lumeng CN, Bodzin JL, Saltiel AR (2007) Obesity induces a phenotypic switch in adipose tissue macrophage polarization. J Clin Invest 117: 175–184.
26. Lumeng CN, DelProposto JB, Westcott DJ, Saltiel AR (2008) Phenotypic switching of adipose tissue macrophages with obesity is generated by spatiotemporal differences in macrophage subtypes. Diabetes 57: 3239–3246.
27. Cinti S, Mitchell G, Barbatelli G, Murano I, Ceresi E, et al. (2005) Adipocyte death defines macrophage localization and function in adipose tissue of obese mice and humans. J Lipid Res 46: 2347–2355.
28. Apovian CM, Bigornia S, Mott M, Meyers MR, Ulloor J, et al. (2008) Adipose macrophage infiltration is associated with insulin resistance and vascular endothelial dysfunction in obese subjects. Arterioscler Thromb Vasc Biol 28: 1654–1659.
29. Bremer AA, Devaraj S, Afify A, Jialal I (2011) Adipose tissue dysregulation in patients with metabolic syndrome. J Clin Endocrinol Metab 96: E1782–1788.
30. Sakaida I, Terai S, Yamamoto N, Aoyama K, Ishikawa T, et al. (2004) Transplantation of bone marrow cells reduces CCl_4-induced liver fibrosis in mice. Hepatology 40: 1304–1311.
31. Van Rooijen N, Sanders A (1994) Liposome mediated depletion of macrophages: mechanism of action, preparation of liposomes and applications. J Immunol Methods 174: 83–93.
32. Itoh M, Suganami T, Satoh N, Tanimoto-Koyama K, Yuan X, et al. (2007) Increased adiponectin secretion by highly purified eicosapentaenoic acid in rodent models of obesity and human obese subjects. Arterioscler Thromb Vasc Biol 27: 1918–1925.
33. Terai S, Ishikawa T, Omori K, Aoyama K, Marumoto Y, et al. (2006) Improved liver function in patients with liver cirrhosis after autologous bone marrow cell infusion therapy. Stem Cells 24: 2292–2298.
34. Juluri R, Vuppalanchi R, Olson J, Unalp A, Van Natta ML, et al. (2010) Generalizability of the Nonalcoholic Steatohepatitis Clinical Research Network Histologic Scoring System for Nonalcoholic Fatty Liver Disease. J Clin Gastroenterol 45: 55–58.
35. Magness ST, Bataller R, Yang L, Brenner DA (2004) A dual reporter gene transgenic mouse demonstrates heterogeneity in hepatic fibrogenic cell populations. Hepatology 40: 1151–1159.
36. Cassiman D, Libbrecht L, Desmet V, Denef C, Roskams T (2002) Hepatic stellate cell/myofibroblast subpopulations in fibrotic human and rat livers. J Hepatol 36: 200–209.
37. Zeisberg M, Yang C, Martino M, Duncan MB, Rieder F, et al. (2007) Fibroblasts derive from hepatocytes in liver fibrosis via epithelial to mesenchymal transition. J Biol Chem 282: 23337–23347.
38. Ma KL, Ruan XZ, Powis SH, Chen Y, Moorhead JF, et al. (2008) Inflammatory stress exacerbates lipid accumulation in hepatic cells and fatty livers of apolipoprotein E knockout mice. Hepatology 48: 770–781.
39. Miura K, Kodama Y, Inokuchi S, Schnabl B, Aoyama T, et al. (2010) Toll-like receptor 9 promotes steatohepatitis by induction of interleukin-1b in mice. Gastroenterology 139: 323–334 e327.
40. Rivera CA, Bradford BU, Hunt KJ, Adachi Y, Schrum LW, et al. (2001) Attenuation of CCl_4-induced hepatic fibrosis by $GdCl_3$ treatment or dietary glycine. Am J Physiol Gastrointest Liver Physiol 281: G200–207.
41. Thomas JA, Pope C, Wojtacha D, Robson AJ, Gordon-Walker TT, et al. (2011) Macrophage therapy for murine liver fibrosis recruits host effector cells improving fibrosis, regeneration, and function. Hepatology 53: 2003–2015.
42. Iwamoto T, Terai S, Hisanaga T, Takami T, Yamamoto N, et al. (2013) Bone-marrow-derived cells cultured in serum-free medium reduce liver fibrosis and improve liver function in carbon-tetrachloride-treated cirrhotic mice. Cell Tissue Res 351: 487–495.
43. Patsouris D, Li PP, Thapar D, Chapman J, Olefsky JM, et al. (2008) Ablation of CD11c-positive cells normalizes insulin sensitivity in obese insulin resistant animals. Cell Metab 8: 301–309.
44. Medzhitov R (2008) Origin and physiological roles of inflammation. Nature 454: 428–435.
45. Asanuma T, Ono M, Kubota K, Hirose A, Hayashi Y, et al. (2010) Super paramagnetic iron oxide MRI shows defective Kupffer cell uptake function in non-alcoholic fatty liver disease. Gut 59: 258–266.
46. Rensen SS, Slaats Y, Nijhuis J, Jans A, Bieghs V, et al. (2009) Increased hepatic myeloperoxidase activity in obese subjects with nonalcoholic steatohepatitis. Am J Pathol 175: 1473–1482.
47. Ioannou GN, Haigh WG, Thorning D, Savard C (2013) Hepatic cholesterol crystals and crown-like structures distinguish NASH from simple steatosis. J Lipid Res 54: 1326–1334.
48. Brunt EM (2010) Pathology of nonalcoholic fatty liver disease. Nat Rev Gastroenterol Hepatol 7: 195–203.
49. Tiniakos DG, Vos MB, Brunt EM (2010) Nonalcoholic fatty liver disease: pathology and pathogenesis. Annu Rev Pathol 5: 145–171.
50. Kleiner DE (2006) Granulomas in the liver. Semin Diagn Pathol 23: 161–169.
51. Caballero T, Gila A, Sanchez-Salgado G, Munoz de Rueda P, Leon J, et al. (2012) Histological and immunohistochemical assessment of liver biopsies in morbidly obese patients. Histol Histopathol 27: 459–466.
52. Fotiadu A, Gagalis A, Akriviadis E, Kotoula V, Sinakos E, et al. (2010) Clinicopathological correlations in a series of adult patients with non-alcoholic fatty liver disease. Pathol Int 60: 87–92.

Yorihiro Iwasaki,[1,4] Takayoshi Suganami,[2,8] Rumi Hachiya,[1,9] Ibuki Shirakawa,[2] Misa Kim-Saijo,[1] Miyako Tanaka,[1] Miho Hamaguchi,[1] Takako Takai-Igarashi,[5] Michikazu Nakai,[6] Yoshihiro Miyamoto,[6,7] and Yoshihiro Ogawa[1,3]

Activating Transcription Factor 4 Links Metabolic Stress to Interleukin-6 Expression in Macrophages

Chronic inflammation is a molecular element of the metabolic syndrome and type 2 diabetes. Saturated fatty acids (SFAs) are considered to be an important proinflammatory factor. However, it is still incompletely understood how SFAs induce proinflammatory cytokine expression. Hereby we report that activating transcription factor (ATF) 4, a transcription factor that is induced downstream of metabolic stresses including endoplasmic reticulum (ER) stress, plays critical roles in SFA-induced interleukin-6 (*Il6*) expression. DNA microarray analysis using primary macrophages revealed that the ATF4 pathway is activated by SFAs. Haploinsufficiency and short hairpin RNA–based knockdown of ATF4 in macrophages markedly inhibited SFA- and metabolic stress–induced *Il6* expression. Conversely, pharmacological activation of the ATF4 pathway and overexpression of ATF4 resulted in enhanced *Il6* expression. Moreover, ATF4 acts in synergy with the Toll-like receptor-4 signaling pathway, which is known to be activated by SFAs. At a molecular level, we found that ATF4 exerts its proinflammatory effects through at least two different mechanisms: ATF4 is involved in SFA-induced nuclear factor-κB activation; and ATF4 directly activates the *Il6* promoter. These findings provide evidence suggesting that ATF4 links metabolic stress and *Il6* expression in macrophages.

Diabetes 2014;63:152–161 | DOI: 10.2337/db13-0757

[1]Department of Molecular Endocrinology and Metabolism, Graduate School of Medical and Dental Sciences, Tokyo Medical and Dental University, Tokyo, Japan
[2]Department of Organ Network and Metabolism, Graduate School of Medical and Dental Sciences, Tokyo Medical and Dental University, Tokyo, Japan
[3]Global Center of Excellence Program, International Research Center for Molecular Science in Tooth and Bone Diseases, Tokyo Medical and Dental University, Tokyo, Japan
[4]Center for Diabetes and Endocrinology, The Tazuke Kofukai Medical Research Institute, Kitano Hospital, Osaka, Japan
[5]Department of Health Record Informatics, Tohoku Medical Megabank Organization, Tohoku University, Miyagi, Japan
[6]Department of Preventive Medicine and Epidemiologic Informatics, National Cerebral and Cardiovascular Center, Osaka, Japan
[7]Department of Preventive Cardiology, National Cerebral and Cardiovascular Center, Osaka, Japan
[8]Precursory Research for Embryonic Science and Technology, Japan Science and Technology Agency, Tokyo, Japan
[9]Japan Society for the Promotion of Science for Young Scientists, Tokyo, Japan

Corresponding author: Takayoshi Suganami, suganami.mem@tmd.ac.jp, or Yoshihiro Ogawa, ogawa.mem@tmd.ac.jp.

Received 10 May 2013 and accepted 26 August 2013.

This article contains Supplementary Data online at http://diabetes.diabetesjournals.org/lookup/suppl/doi:10.2337/db13-0757/-/DC1.

See accompanying commentary, p. 48.

Chronic inflammation is a molecular element of the metabolic syndrome and type 2 diabetes. Several proinflammatory signaling pathways, including interleukin 6 (IL-6) signaling, are shown to play essential roles in the pathophysiology of the metabolic syndrome, type 2 diabetes, and subsequent cardiovascular diseases (1–3). As a causative factor of chronic inflammation, several lines of evidence support the role of free fatty acids. Of note, saturated fatty acids (SFAs), such as palmitate (Pal) and stearate, have been shown to induce proinflammatory cytokine production in various cell types, including macrophages (4,5). However, the underlying mechanism of SFA-induced proinflammatory cytokine expression is only partially elucidated.

To date, we and others have demonstrated that Toll-like receptor-4 (TLR4), a pathogen sensor expressed on the cell surface, plays a critical role in the SFA-induced proinflammatory cytokine expression (4–6). On the other hand, multiple mechanisms are involved in the SFA-induced cellular responses (1,7,8). Among them, attention has been focused on the role of cellular metabolic stresses such as endoplasmic reticulum (ER) stress and oxidative stress (1). Recent reports suggest that the modulation of metabolic stress pathways may alter high-fat diet–induced proinflammatory cytokine expression as well as insulin resistance (9,10). Therefore, it is of importance to clarify the molecular mechanism by which metabolic stresses affect proinflammatory cytokine expression.

In this study, using DNA microarray and network analyses in macrophages, we show that activating transcription factor (ATF) 4, a basic leucine zipper transcription factor, is potently induced by SFAs. We provide evidence that ATF4 plays essential roles in *Il6* expression induced by various metabolic stresses, including ER stress. Furthermore, the ATF4 pathway has a synergistic effect on the TLR4 signaling pathway, enhancing *Il6* expression. As a molecular mechanism, ATF4 is capable of enhancing metabolic stress–induced nuclear factor-κB (NF-κB) activation and directly activating the *Il6* promoter. Our data suggest that ATF4 is a novel link between metabolic stress and *Il6* expression in macrophages.

RESEARCH DESIGN AND METHODS

Mice, Cells, and Reagents

Tlr4- and *Atf4*-deficient mice were provided by Dr. Shizuo Akira (Osaka University, Osaka, Japan). Mice were maintained on the C57BL/6 (B6) genetic background. All animal experiments were performed in accordance with the guidelines of Tokyo Medical and Dental University (no. 2011–207C, no. 0130269A). Murine peritoneal and bone marrow–derived macrophages (BMDMs) were prepared as described (11). All primary cells used for in vitro experiments were on the B6 background. Splenic CD11b–positive cells were purified using anti-CD11b magnetic beads and LS-columns (Miltenyi Biotec, Bergisch Gladbach, Germany). The RAW264 macrophage cell line (RIKEN BioResource Center, Tsukuba, Japan) was maintained in Dulbecco's modified Eagle's medium (Nacalai Tesque, Kyoto, Japan) containing 10% FBS. Palmitate (P5585), stearate (P4751), lipopolysaccharide (LPS; P4391), lipid A (L5399), and a double-stranded RNA–dependent protein kinase (PKR) inhibitor (2-aminopurine; A3509) were purchased from Sigma-Aldrich (St. Louis, MO). Fatty acids were solubilized in ethanol, and conjugated with fatty acid-free and Ig-free BSA at a molar ratio of 10:1 (fatty acid/albumin) in serum-poor medium (0.5% FBS) (4). The vehicle control used was a mixture of ethanol and BSA alone in place of fatty acids. A PKR-like ER kinase (PERK) inhibitor (GSK2606414) was obtained from EMD Millipore (Calbiochem; Billerica, MA). A stearoyl-CoA desaturase 1 inhibitor (A939572) was from BioVision (Milpitas, CA). Antibodies against ATF4 (sc200), RelA (sc372), ATF3 (sc188), β-actin (sc47778), and Lamin A/C (sc20681) were from Santa Cruz Biotechnology (Dallas, TX). Antibodies against IκBα (catalog #9242), eukaryotic initiation factor-2α (eIF2α; catalog #9722), and phospho-eIF2α (catalog #9721) were from Cell Signaling Technology (Danvers, MA). An antibody against ATF6 (IMG273) was from Imgenex (San Diego, CA).

Microarray, Network, and Pathway Analyses

Total RNAs were extracted from thioglycollate-elicited peritoneal macrophages using the RNeasyMini Kit (Qiagen, Valencia, CA). Microarray analysis was performed on biological duplicate samples using Affymetrix GeneChip Mouse Genome 430 2.0 Arrays according to the manufacturer's instructions (12). Genes with an average fold change >1.8 and labeled as both "present (P)" and "increased (I)" were considered to be differentially upregulated. Affymetrix probe IDs were converted to unique Entrez IDs. Protein networks were built running the Markov clustering algorithm using the functional and physical interaction scores from STRING 9.0 with an inflation parameter of 2.0. Markov clustering has been used by many groups to build protein complexes or families based on protein-protein interactions (13,14). The results were visualized in Cytoscape software (15). Pathway and gene ontology analyses were performed using the Reactome functional protein interaction database (http://www.reactome.org/).

Nuclear Cytoplasmic Fractionation

The cells were collected in ice-cold PBS, resuspended in buffer A (10 mmol/L HEPES-KOH at pH 7.8, 10 mmol/L KCl, 0.1 mmol/L EDTA, 1 mmol/L dithiothreitol, 0.5 mmol/L phenylmethylsulfonyl fluoride, and protease inhibitors) and incubated on ice for 5 min. The cells were then spun down, and the cytoplasmic fraction was aspirated to separate tubes. The nuclear fraction was then lysed in buffer C (50 mmol/L HEPES-KOH at pH 7.8,

420 mmol/L KCl, 0.1 mmol/L EDTA, 5 mmol/L $MgCl_2$, 1 mmol/L dithiothreitol, 0.5 mmol/L phenylmethylsulfonyl fluoride, and protease inhibitors) at 4°C for 30 min. The lysate was clarified by centrifugation, and the supernatant was collected.

Chromatin Immunoprecipitation Assay

Chromatin immunoprecipitation was performed using the MAGnify Chromatin Immunoprecipitation System (49–2024; Invitrogen, Carlsbad, CA) according to the manufacturer's instructions with some modifications. In brief, thioglycollate-elicited peritoneal macrophages were cross-linked with 1% (w/v) formaldehyde for 10 min and lysed in the buffer provided. Nuclear extracts from 3×10^6 to 1×10^7 cells were used per immunoprecipitation reaction. Sonicated nuclear extracts were immunoprecipitated for 2 h at 4°C with anti-ATF4 (sc200x, 3 μg), anti-RelA (sc372, 3 μg), or IgG isotype negative control (sc2027, 3 μg) antibodies (Santa Cruz Biotechnology). DNA was eluted and purified as previously described (16). Eluted DNA was quantified with quantitative PCR using SYBR GREEN chemistry (StepOne Plus; Applied Biosystems, Foster City, CA).

RNA Purification, Reverse Transcription, and Real-Time PCR Amplification

RNA was purified using Sepasol (30486–56; Nacalai Tesque), according to the manufacturer's instructions. Total RNA (1.25 μg) was reverse-transcribed using a ReverTraAce (FSQ-201; Toyobo, Osaka, Japan). Ten nanograms of cDNA were used for real-time PCR amplification with SYBR GREEN detection protocol in a thermal cycler (StepOne Plus; Applied Biosystems). Data were normalized to the 36B4 levels and analyzed using the comparative threshold cycle method (12). Primer sequences are listed in Supplementary Table 1.

Plasmid Construction, Transfection, and Knockdown Experiments

An expression vector encoding murine ATF4 was constructed by inserting PCR-amplified cDNA fragment encoding ATF4 between the *Eco*RI and *Bam*HI sites of the pcDNA3.1Myc-His3 expression vector. For generation of the ATF4 5′ untranslated region (UTR) luciferase reporter plasmid, the 285 base pairs of murine ATF4 5′ UTR was amplified by PCR and was inserted into the *Hin*dIII site of the pGL3 control vector (E1741; Promega, Madison, WI). The rat *Il6* promoter luciferase reporter plasmid and various truncated constructs (17) were gifts from Dr. Toshihiro Ichiki (Kyushu University, Fukuoka, Japan). The *Il6* promoter construct containing mutant ATF/cAMP-responsive element–binding protein site was generated from the *Il6* promoter construct 2 by the inverse PCR-based site-directed mutagenesis using KOD plus DNA polymerase (KOD201; Toyobo). The thymidine-kinase promoter renilla luciferase reporter vector was purchased from Promega. All transfection experiments were performed using Lipofectamine LTX reagent (A12621; Invitrogen) according to the manufacturer's protocol. Retrovirus-mediated knockdown of ATF4 was performed as previously described (18). The target sequences for short hairpin (sh) ATF4 were 5′-TCCCTCCATGTGTAAAGGA-3′ (shATF4 1) and 5′-CTCTGTTTCGAATGGATGA-3′ (shATF4 2), respectively. As a negative control, shGFP was used as described previously (18).

Luciferase Assay

For the ATF4 5′ UTR luciferase assay, RAW264 macrophages seeded on 24-well plates were transiently cotransfected with 30 ng renilla and 600 ng firefly luciferase reporter plasmids. For the *Il6* promoter luciferase assay RAW264 macrophages were transiently cotransfected with 50 ng renilla and 250 ng firefly luciferase reporter plasmids. Twenty-four hours after transfection, cells were collected and luciferase activity was measured with a dual-luciferase reporter assay system (Promega) according to the manufacturer's protocol. All data were normalized for transfection efficiency by the division of firefly luciferase activity by renilla luciferase activity.

NF-κB RelA DNA-Binding Activity Assay

Ten micrograms of nuclear extracts was used to determine RelA (p65) DNA–binding activity using an ELISA-based assay (TransAM 40096; Active Motif, Carlsbad, CA), according to the manufacturer's instructions. In brief, κB oligonucleotide–coated plates (in a 96-well format) were incubated for 1 h with the nuclear extracts. Specificity was achieved by incubation with anti-RelA primary antibodies for 1 h. Horseradish peroxidase–conjugated secondary antibodies were used for the detection of RelA bound to the κB sequences.

ELISA

ELISA of mouse IL-6 was performed using Mouse IL-6 Quantikine ELISA Kit (R&D Systems, Minneapolis, MN), as described previously (19).

Statistical Analysis

Data were expressed as the mean ± SEM. *P* values were calculated using two-tailed Student *t* tests.

RESULTS

ATF4 Pathway Is Activated by SFAs in the Absence of TLR4

In an attempt to identify novel mechanisms underlying the SFA-induced inflammatory responses, we performed DNA microarray analysis of palmitate-stimulated peritoneal macrophages obtained from *Tlr4*-deficient and wild-type mice. A total of 122 genes were upregulated by palmitate in both *Tlr4*-deficient and wild-type macrophages (Fig. 1*A*). We next performed Markov clustering of these genes using STRING database (20), which produced several clusters (Fig. 1*B*). Pathway analysis using the Reactome database (21) identified two large clusters

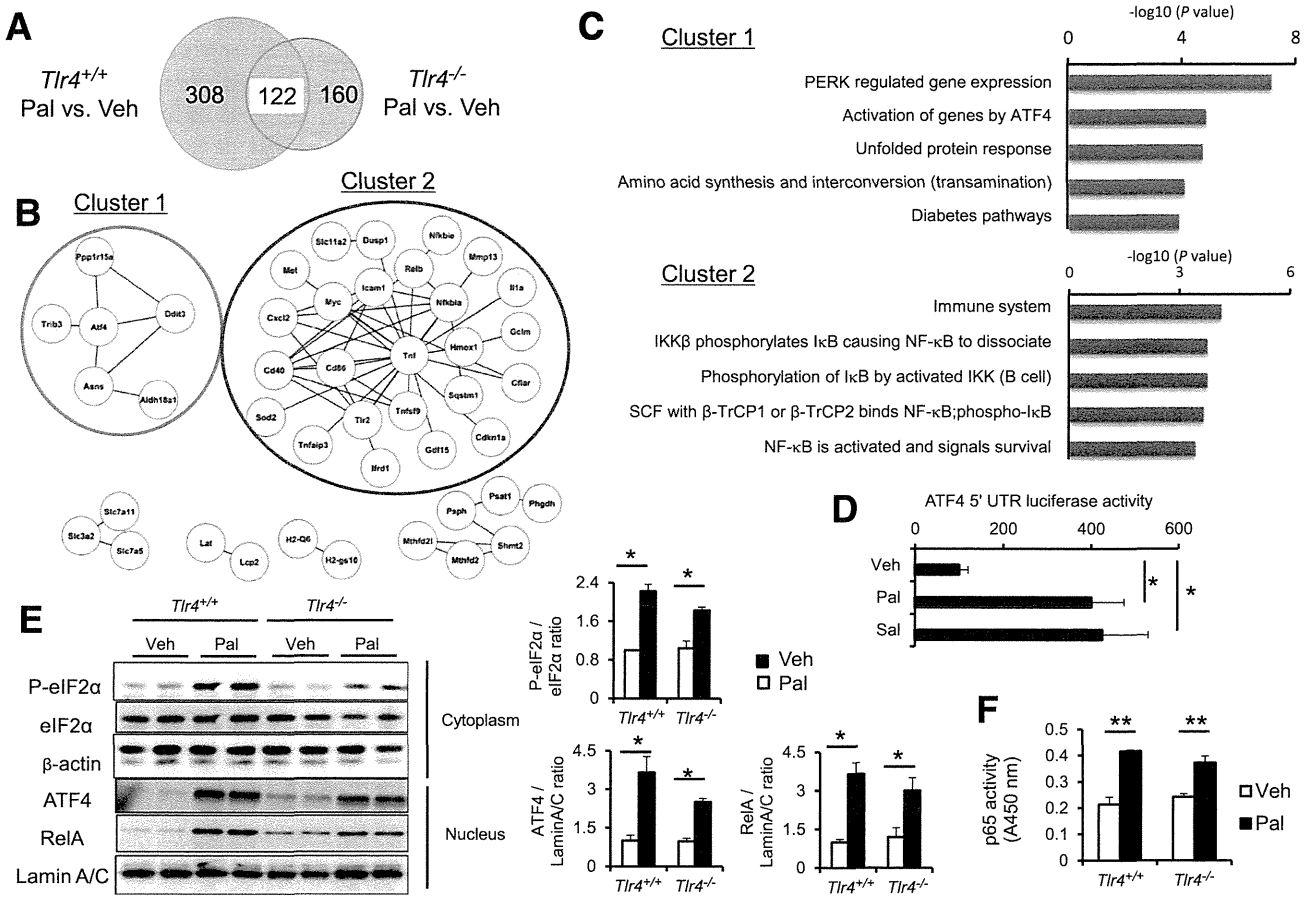

Figure 1—The ATF4 pathway is activated by SFAs in the absence of TLR4. *A*: Venn diagram showing genes induced by palmitate (Pal) in a TLR4-independent manner. $Tlr4^{+/+}$ and $Tlr4^{-/-}$ peritoneal macrophages were treated with 500 μmol/L Pal or BSA (Veh) for 8 h. *B*: Network analysis of the 122 genes in the overlap in *A* on the STRING 9.0 database interaction network, followed by Markov clustering algorithm. *C*: Pathway analysis of the clusters formed in *B* using the Reactome database. *D*: Activation of ATF4 translation by Pal. RAW264 cells were transiently transfected with the ATF4 5′ UTR luciferase construct. Cells were stimulated with 500 μmol/L Pal, 20 μmol/L Sal (used as a positive control) or Veh for 8 h (*$P < 0.05$, $n = 3$). *E*: Western blotting of cytoplasmic (for P-eIF2α, eIF2α, and beta-actin) and nuclear (for ATF4, RelA, and lamin A/C) fractions of $Tlr4^{+/+}$ and $Tlr4^{-/-}$ peritoneal macrophages. Cells were stimulated with 500 μmol/L Pal or Veh for 8 h. Representative blots (*left*) and quantitative results (*right*) are shown (*$P < 0.05$, $n = 5$). *F*: NF-κB activity assay. $Tlr4^{+/+}$ and $Tlr4^{-/-}$ peritoneal macrophages were treated with 500 μmol/L Pal or Veh for 4 h. NF-κB p65/RelA activity in the nuclear extract was measured (**$P < 0.01$, $n = 3$). IKK, inhibitor of nuclear factor κB kinase; IκB, inhibitor of nuclear factor κB; SCF, Skp1-cullin-F-box protein; β-TrCP, β-transducin repeat-containing protein.

in which target genes for ATF4 and NF-κB were enriched (Fig. 1*C*). Indeed, several signaling pathways that can induce ATF4 were significantly enriched in gene ontology analysis (Supplementary Fig. 1).

ATF4 is induced following phosphorylation of eIF2α, which is mediated by eIF2α kinases (i.e., the heme-regulated eIF2α kinase, PKR, PERK, and the general control nonderepressible 2) under metabolic stresses such as ER stress, oxidative stress, and amino acid deprivation (22). Previous reports showed that at least two of the eIF2α kinases, PKR and PERK, are activated by SFAs (9,23). Consistently, pharmacological inhibitors of PKR and PERK suppressed palmitate-induced activation of the ATF4 pathway (Supplementary Fig. 2*A* and *B*), suggesting that PKR and PERK are likely to be involved in SFA-induced eIF2α phosphorylation. When eIF2α is phosphorylated, ATF4 translation is preferentially upregulated through the characteristic upstream open reading frames in the 5′ UTR (24). Using ATF4 5′ UTR luciferase assay, we confirmed that ATF4 translation was activated by palmitate in RAW264 macrophage–like cell lines (Fig. 1*D*). In line with this, palmitate increased ATF4 protein levels and the expression of target genes, such as tribbles homolog-3 (*Trib3*) and c/ebp homologous protein (*Chop*, also known as *Ddit3*) (25), in peritoneal macrophages, at least in part, independent of TLR4 (Fig. 1*E*, and Supplementary Fig. 2*D*). We also observed that other branches of the unfolded protein response were activated by palmitate in the absence of TLR4 (Supplementary Fig. 2*C* and *D*). Intriguingly, we found that, even in *Tlr4*-deficient macrophages, palmitate increased the expression of some proinflammatory cytokines, such as *Il6* and tumor necrosis factor (*Tnf*), to a lesser extent than wild-type macrophages (Supplementary Fig. 2*D*). Consistent

with this, nuclear protein levels and activity of RelA (p65), a transcriptional activating subunit of NF-κB, were increased by palmitate in both wild-type and *Tlr4*-deficient macrophages (Fig. 1*E* and *F*). These results suggest that the ATF4 pathway, as well as the NF-κB pathway, is activated in macrophages by palmitate in the absence of TLR4.

In addition, we confirmed that stearate, another SFA, also activated the ATF4 pathway in RAW264 macrophages (Supplementary Fig. 3*A*). By contrast, unsaturated fatty acids such as oleate and eicosapentaenoic acid did not activate the ATF4 pathway (Supplementary Fig. 3*B*). Notably, eicosapentaenoic acid effectively suppressed palmitate-induced activation of the ATF4 pathway (Supplementary Fig. 3*B*). We also found that pharmacological inhibition of fatty acid desaturation resulted in upregulation of ATF4 target genes (Supplementary Fig. 3*C*) (26,27), suggesting that intracellular SFAs, not unsaturated fatty acids, play a role in the ATF4 pathway activation. Although further studies are required, our results are consistent with previous reports showing that altered membrane lipid composition may activate unfolded protein response pathways through several mechanisms, including calcium depletion (28) and direct activation of ER membrane sensors (29).

ATF4 Is Required for *Il6* Expression in Response to Metabolic Stresses

In contrast to NF-κB (30), the role of ATF4 in the inflammatory pathway is not yet fully characterized. Because *Atf4*-null mice are mostly embryonic or neonatal lethal (31), in this study we used primary macrophages obtained from *Atf4*-haploinsufficient mice. We found that BMDMs from *Atf4*-haploinsufficient mice were defective in palmitate-induced mRNA expression of *Il6* (Fig. 2*A*). *Tnf* expression was only marginally attenuated

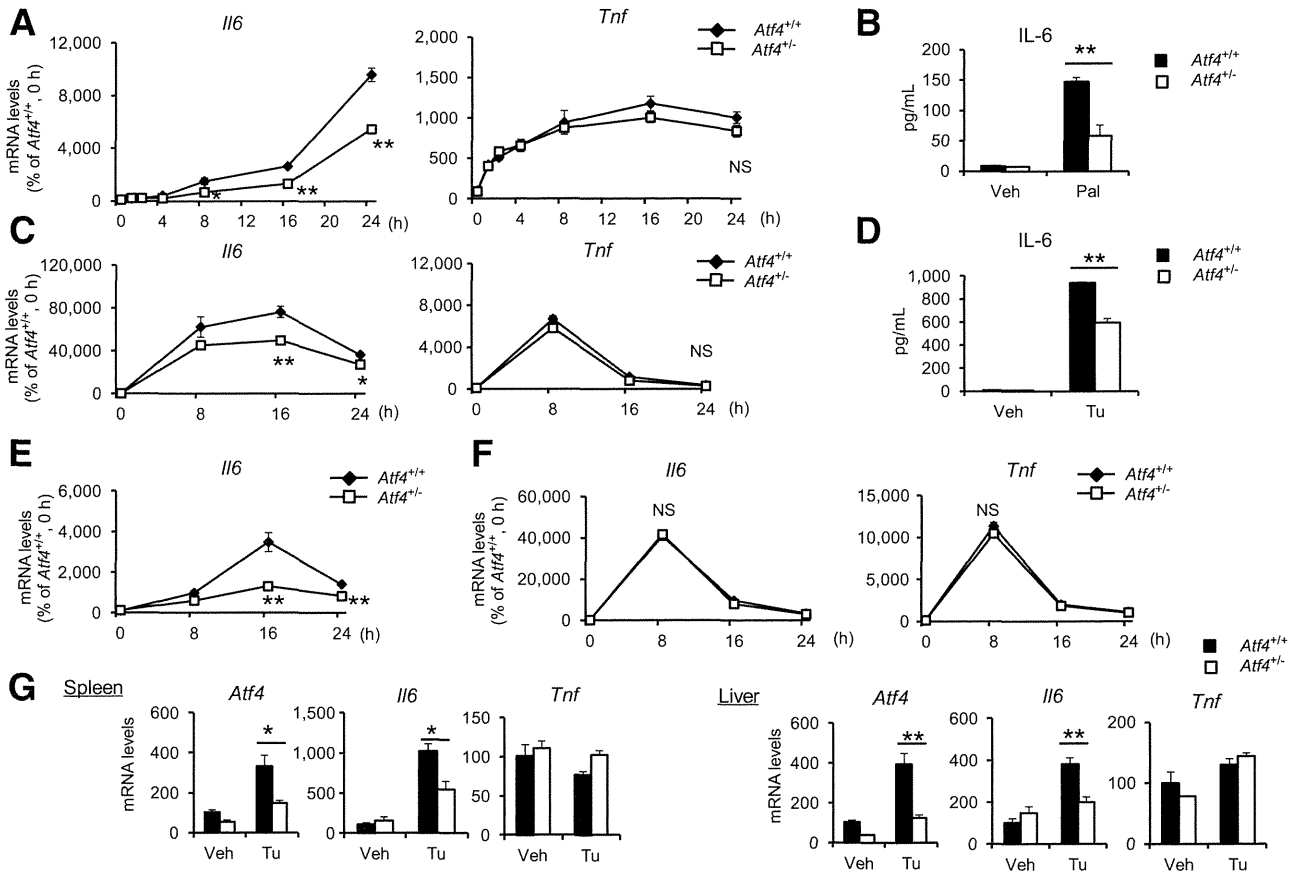

Figure 2—ATF4 is required for *Il6* expression in response to metabolic stresses. *A* and *B*: $Atf4^{+/+}$ and $Atf4^{+/-}$ BMDMs were treated with 500 μmol/L palmitate (Pal) or BSA (Veh). *A*: Expression levels of proinflammatory cytokines at the indicated time points (*$P < 0.05$, **$P < 0.01$, $n = 3$). *B*: IL-6 levels in the culture media obtained from 24-h treated samples (**$P = 0.0094$, $n = 3$). *C* and *D*: $Atf4^{+/+}$ and $Atf4^{+/-}$ peritoneal macrophages were treated with 1 μg/mL tunicamycin (Tu) or DMSO (Veh). *C*: Expression levels of proinflammatory cytokines at the indicated time points (*$P < 0.05$, **$P < 0.01$, $n = 3$). *D*: IL-6 levels in the culture media obtained from 24-h treated samples (**$P = 0.0006$, $n = 3$). *E* and *F*: Expression levels of proinflammatory cytokines were measured at the indicated time points. *E*: $Atf4^{+/+}$ and $Atf4^{+/-}$ peritoneal macrophages were treated with 1 μmol/L thapsigargin (**$P < 0.01$, $n = 3$). *F*: $Atf4^{+/+}$ and $Atf4^{+/-}$ peritoneal macrophages were treated with 10 ng/mL lipid A ($n = 3$). *G*: $Atf4^{+/+}$ and $Atf4^{+/-}$ mice were intraperitoneally injected with Tu 1 mg/kg or DMSO (Veh). Sixteen hours after injection, expression levels of *Atf4* and proinflammatory cytokines were examined in the spleen and the liver (*$P < 0.05$, **$P < 0.01$, $n = 5$).

in *Atf4*-haploinsufficient macrophages. Consistently, *Atf4*-haploinsufficient macrophages showed decreased secretion of IL-6 in the media (Fig. 2*B*). Similarly, *Atf4*-haploinsufficient peritoneal macrophages showed attenuated *Il6* expression induced by ER stressors, such as tunicamycin (Fig. 2*C* and *D*) and thapsigargin (Fig. 2*E*), compared with wild-type macrophages. To test the importance of ATF4 in RAW264 macrophages, we knocked down *Atf4*, which was confirmed by quantitative PCR and Western blotting (Supplementary Fig. 4*A* and *B*). *Atf4* knockdown reduced SFA-induced (Supplementary Fig. 4*C*) or ER stress–induced (Supplementary Fig. 4*D*) *Il6* expression. On the other hand, in macrophages treated without these stressors, there was no significant difference in lipid A (a bona fide TLR4 ligand)–induced proinflammatory cytokine expression between the genotypes (Fig. 2*F*). To test the in vivo functional role of ATF4, we activated the ATF4 pathway by intraperitoneal injection of tunicamycin (Fig. 2*G*). Sixteen hours after the injection, tunicamycin treatment potently induced

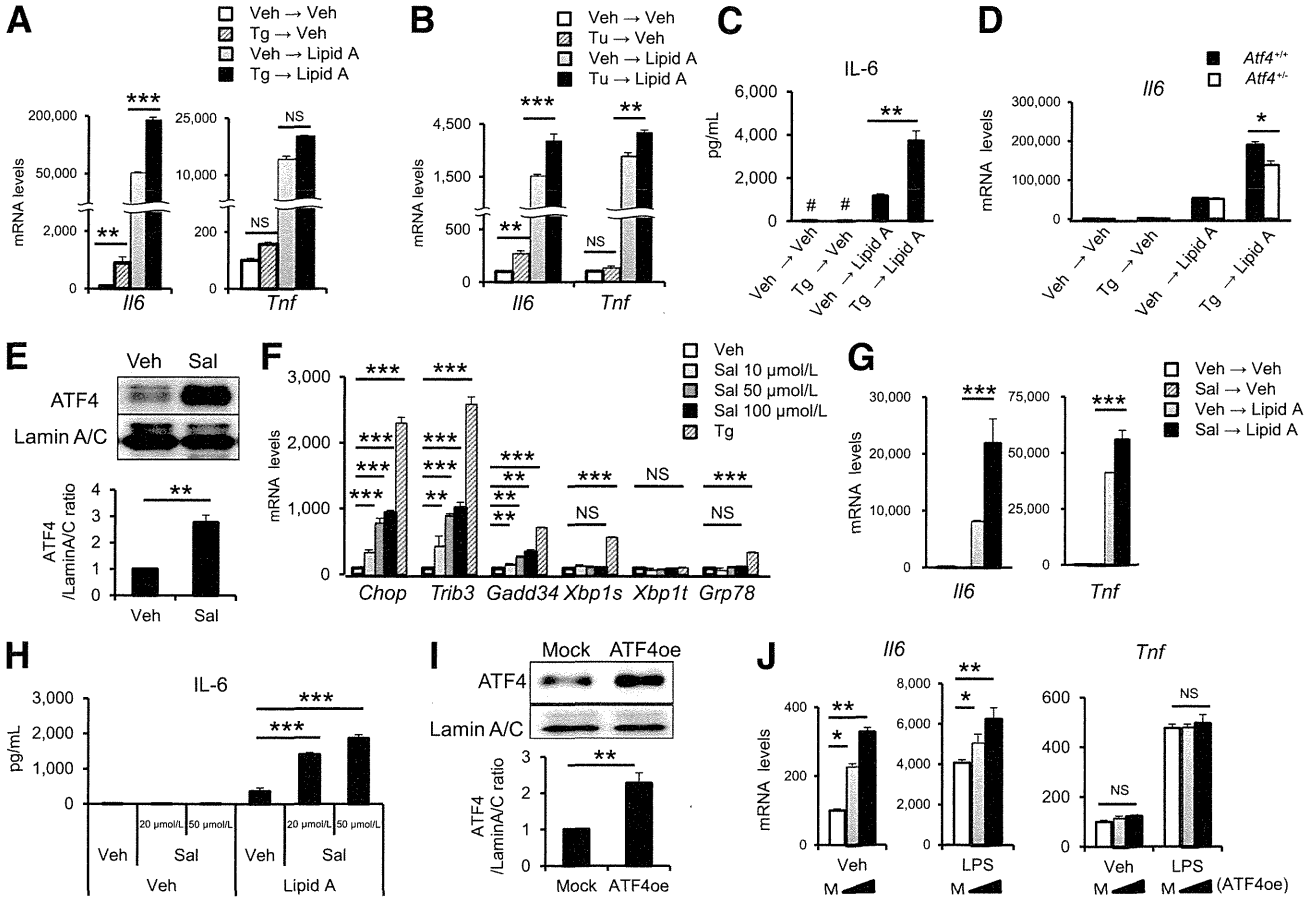

Figure 3—Activation of the ATF4 pathway exaggerates *Il6* expression in synergy with the TLR4 pathway. *A* and *B*: Expression levels of proinflammatory cytokines were measured. *A*: BMDMs were pretreated with 1 μmol/L thapsigargin (Tg) or DMSO (Veh) for 2 h, then stimulated with 10 ng/mL lipid A or PBS (Veh) for 4 h (**$P < 0.01$, ***$P < 0.001$, $n = 3$). *B*: Peritoneal macrophages were pretreated with 1 ng/mL tunicamycin (Tu) or DMSO (Veh) for 2 h, then stimulated with 10 ng/mL lipid A or PBS (Veh) for 4 h (**$P < 0.01$, ***$P < 0.001$, $n = 3$). *C*: RAW264 macrophages were pretreated with 0.3 μmol/L Tg or DMSO (Veh) for 2 h, then stimulated with 10 ng/mL lipid A or PBS (Veh) for 4 h. IL-6 levels in the culture media were measured by ELISA (**$P = 0.0017$, $n = 4$; #below the lower limit of quantification). *D*: $Atf4^{+/+}$ and $Atf4^{+/-}$ BMDMs were pretreated with 1 μmol/L Tg or DMSO (Veh) for 2 h, then stimulated with 10 ng/mL lipid A or PBS (Veh) for 4 h. Expression levels of proinflammatory cytokines were measured (*$P = 0.0182$, $n = 3$). *E*: RAW264 macrophages were treated with 20 μmol/L Sal or DMSO (Veh) for 4 h. ATF4 protein levels in the nucleus was determined by Western blotting. Representative blots (*top*) and quantitative results (*bottom*) are shown (**$P < 0.01$, $n = 4$). *F* and *G*: Expression levels of proinflammatory cytokines were measured. *F*: RAW264 macrophages were treated with Sal (10, 50, 100 μmol/L) or 1 μmol/L Tg or DMSO (Veh) for 4 h (**$P < 0.01$, ***$P < 0.001$, $n = 3$). *G*: BMDMs were pretreated with 50 μmol/L Sal or DMSO (Veh) for 4 h, then stimulated with 10 ng/mL lipid A or PBS (Veh) for 4 h (***$P < 0.001$, $n = 3$). *H*: BMDMs were pretreated with Sal 20 and 50 μmol/L or DMSO (Veh) for 4 h, then stimulated with 10 ng/mL lipid A or PBS (Veh) for 4 h. IL-6 levels in the culture media were measured (***$P < 0.001$, $n = 3$). *I* and *J*: RAW264 macrophages were transiently transfected with expression vectors encoding murine ATF4 (ATF4oe) or empty vectors (Mock or M). *I*: Twenty-four hours after transfection, ATF4 protein levels in the nucleus were determined by Western blotting. Representative blots (*top*) and quantitative results (*bottom*) are shown (**$P < 0.01$, $n = 4$). *J*: Twenty-four hours after transfection, cells were stimulated with 100 ng/mL LPS or PBS (Veh) for 4 h. Expression levels of proinflammatory cytokines were measured (*$P < 0.05$, **$P < 0.01$, $n = 3$). *Gadd34*, growth arrest and DNA damage-inducible gene 34; *Grp78*, glucose-regulated protein 78.

Atf4 and *Il6* mRNA expression in the spleen and liver from wild-type mice, which was significantly decreased in those from *Atf4*-haploinsufficient mice. *Tnf* expression was not significantly decreased. We obtained a similar result using purified CD11b-positive splenic macrophages (Supplementary Fig. 5). In this study, we observed no apparent difference in LPS-induced *Il6* mRNA expression between the genotypes (data not shown). These observations suggest that ATF4 plays a critical role in the metabolic stress–induced proinflammatory cytokine expression in vitro and in vivo.

ATF4 Pathway Enhances *Il6* Expression in Synergy With the TLR4 Pathway

We next examined the impact of the ATF4 pathway activation on proinflammatory cytokine expression in cells under metabolic stresses. Pretreatment of various macrophages with ER stressors markedly enhanced the lipid A–induced mRNA expression and secretion of IL-6 (Fig. 3*A–C* and Supplementary Fig. 6*A*). The expression levels of *Tnf* were also affected to a lesser extent (Fig. 3*A* and *B*). Similar results were obtained using murine embryonic fibroblasts (MEFs) (Supplementary Fig. 6*C*). Although the magnitude varied, the patterns of gene expression in response to ER stressors and TLR4 agonists were similar among cell types. Notably, this enhancement was significantly attenuated in *Atf4*-haploinsufficient macrophages (Fig. 3*D*), ATF4 knockdown RAW264 macrophages (Supplementary Fig. 6*B*), and *Atf4*-deficient MEFs (Supplementary Fig. 6*C*). These observations suggest that the ATF4 pathway has a synergistic effect on the TLR4 signaling pathway.

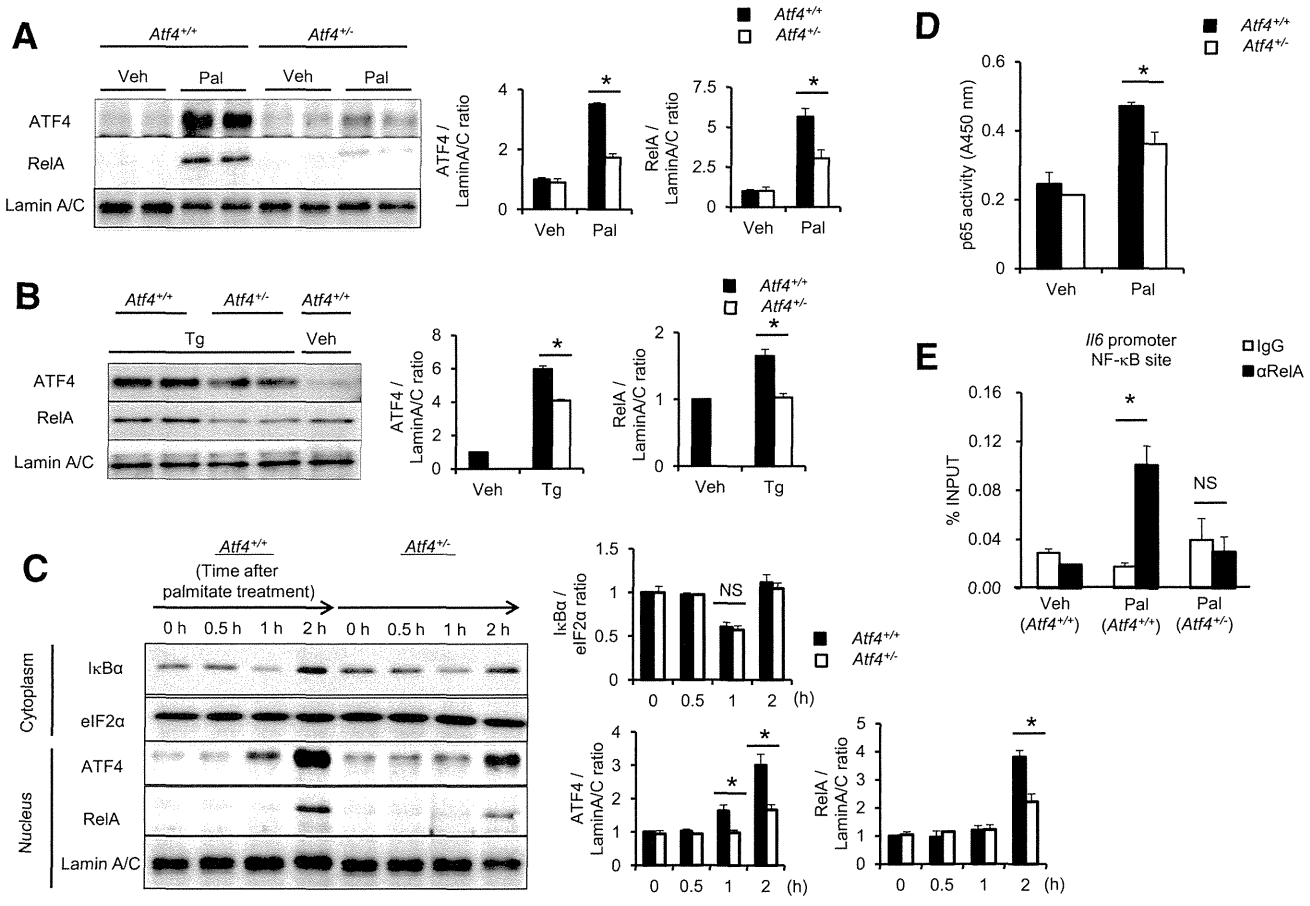

Figure 4—ATF4 is involved in NF-κB activation in response to metabolic stresses. *A* and *B*: Western blotting of nuclear extracts from peritoneal macrophages. Representative blots (*left*) and quantitative results (*right*) are shown (*$P < 0.05$, $n = 4–5$). *A*: Cells were treated with 500 μmol/L palmitate (Pal) or BSA (Veh) for 6 h. *B*: Cells were treated with 1 μmol/L thapsigargin (Tg) or DMSO (Veh) for 2 h. *C*: Earlier kinetics of Pal-induced changes in the NF-κB pathway. Western blotting of cytoplasmic (for IκBα and eIF2α) and nuclear (for ATF4, RelA, and lamin A/C) fractions from peritoneal macrophages treated with 500 μmol/L Pal for indicated times. Representative blots (*left*) and quantitative results (*right*) are shown (*$P < 0.05$, $n = 4$). *D*: NF-κB activity assay. *Atf4*$^{+/+}$ and *Atf4*$^{+/-}$ peritoneal macrophages were treated with 500 μmol/L Pal or BSA (Veh) for 4 h. NF-κB p65/RelA activity in the nuclear extract was measured (*$P = 0.0295$, $n = 3$). *E*: A chromatin immunoprecipitation assay using *Atf4*$^{+/+}$ and *Atf4*$^{+/-}$ peritoneal macrophages. Cells were treated with 500 μmol/L Pal or BSA (Veh) for 4 h (*$P = 0.0349$, $n = 3$). Chromatin was immunoprecipitated and quantitated by PCR analysis of the region neighboring an NF-κB site on the *Il6* promoter. IκBα, inhibitor of nuclear factor κBα.

In addition to the eIF2α-ATF4 branch, ER stress activates two other branches of the unfolded protein response: the inositol requiring enzyme 1α X-box binding protein 1 (XBP1) and ATF6 branches, the former of which is also involved in proinflammatory cytokine expression (32). To specifically stimulate the ATF4 pathway, we used salubrinal (Sal), an inhibitor of eIF2α phosphatase complex (33). Pretreatment of BMDMs with Sal resulted in upregulation of ATF4 (Fig. 3*E*) and its target genes, whereas its effect on XBP1 splicing was minimal (Fig. 3*F*). Moreover, pretreatment with Sal potently enhanced the lipid A–induced mRNA expression and secretion of IL-6 in BMDMs (Fig. 3*G* and *H*) and RAW264 macrophages (Supplementary Fig. 6*D* and *E*). We also examined the effect of amino acid deprivation, another metabolic stress known to activate the ATF4 pathway (34), on *Il6* expression. Pretreatment with azetidine, a proline analog, significantly enhanced the lipid A–induced *Il6* expression (Supplementary Fig. 6*F*). Transient overexpression of ATF4 showed similar effects in RAW264 macrophages (Fig. 3*I* and *J*). These observations confirm that, in addition to the previously characterized XBP1 pathway, the ATF4 pathway is also involved in the regulation of metabolic stress–induced proinflammatory cytokine expression. Of note, a recent report showed that the ATF4 pathway was attenuated following the low-dose treatment of TLR4 ligands in cultured macrophages (34). Collectively, it is conceivable that there is a bidirectional crosstalk between the ATF4 and TLR4 pathways.

ATF4 Is Involved in NF-κB Activation in Response to Metabolic Stresses

We next aimed to clarify the molecular mechanism of the SFA-induced *Il6* expression through the ATF4 pathway. First, we examined the effect of ATF4 on palmitate-induced NF-κB activation, because our microarray analysis revealed that the NF-κB pathway was activated in *Tlr4*-deficient macrophages (Fig. 1*B* and *C*). In this study, we found that the nuclear protein levels and activity of RelA were increased by palmitate even in the absence of TLR4 (Fig. 1*E* and *F*). Interestingly, *Atf4* haploinsufficiency markedly reduced nuclear protein levels of RelA induced by palmitate or thapsigargin in peritoneal macrophages

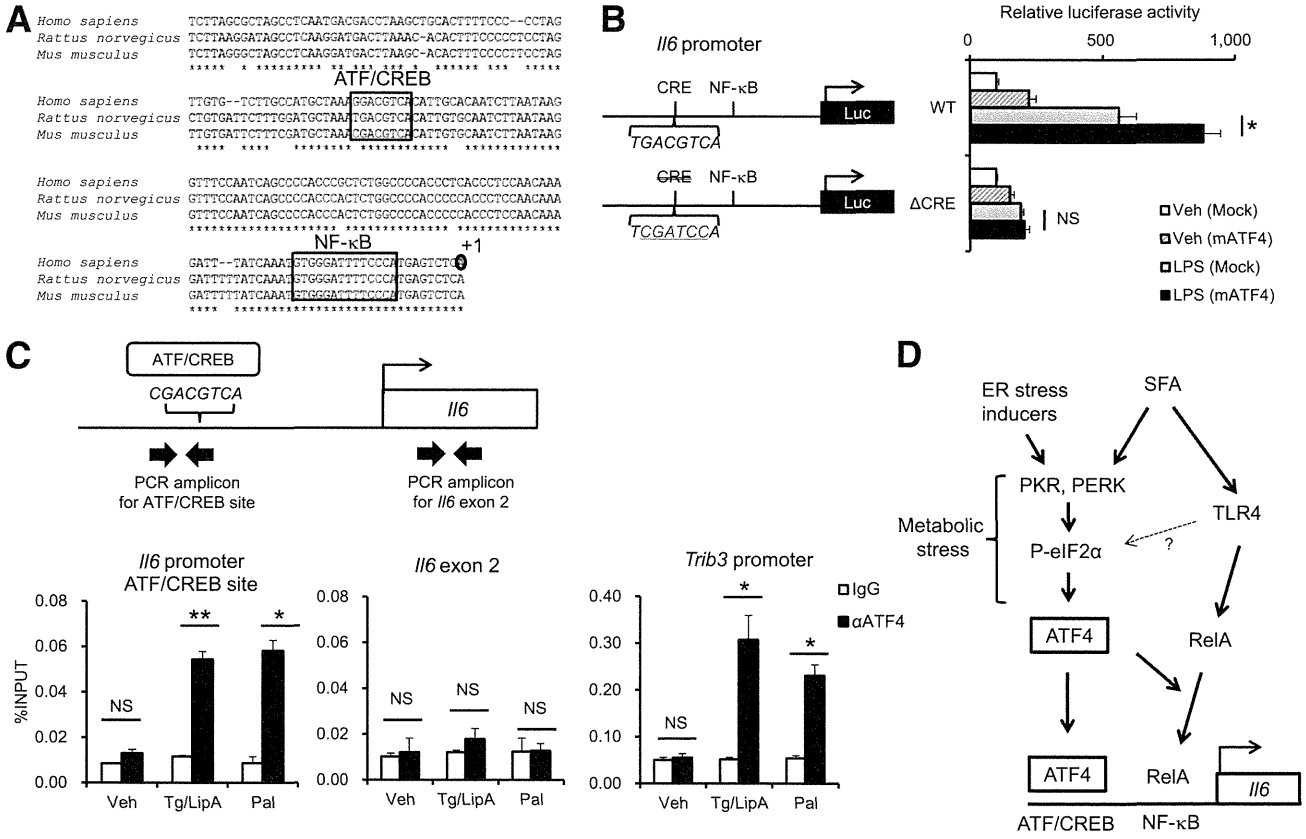

Figure 5—ATF4 directly activates the *Il6* promoter. *A*: The evolutionarily conserved region of the *Il6* promoter. *B*: The *Il6* promoter luciferase (Luc) assay in RAW264 macrophages. Cells were transiently transfected with expression vectors encoding murine ATF4 (mATF4) or empty vectors (Mock). Twenty-four hours after transfection, cells were stimulated with 100 ng/mL LPS for 24 h (*P = 0.0154, n = 3). *C*: A chromatin immunoprecipitation assay using peritoneal macrophages. Cells were treated with BSA for 4 h (Veh), palmitate (Pal) (500 μmol/L) for 4 h, or thapsigargin (Tg) (1 μmol/L) for 2 h followed by lipid A (LipA) (10 ng/mL) for 4 h (*P < 0.05, **P < 0.01, n = 3). Chromatin was immunoprecipitated and quantitated by PCR analysis of the region containing the ATF/CREB site on the *Il6* promoter. *Il6* exon 2 and the *Trib3* promoter were used as negative and positive control loci, respectively. *D*: Schematic representation. WT, wild type.

(Fig. 4*A* and *B*). We next examined the kinetics of cytoplasmic IκBα degradation, a well-recognized event prior to nuclear translocation of RelA (30), and found no apparent difference in cytoplasmic IκBα protein levels between the genotypes (Fig. 4*C*). Moreover, we observed that NF-κB activity induced by palmitate was significantly attenuated in *Atf4*-haploinsufficient macrophages relative to wild-type macrophages (Fig. 4*D*). Consistently, a chromatin immunoprecipitation assay showed decreased recruitment of RelA to the *Il6* promoter region in *Atf4*-haploinsufficient macrophages (Fig. 4*E*). Because the transcriptional activity of RelA can be regulated by multiple mechanisms (30), further studies are required to elucidate how ATF4 affects RelA activity. Although a previous report showed that phosphorylation of eIF2α leads to NF-κB activation in MEFs (35), our data provide novel evidence that ATF4 is involved in metabolic stress–induced NF-κB activation in macrophages.

ATF4 Directly Activates the *Il6* Promoter

On the basis of its potent proinflammatory effect, we next examined whether ATF4 directly activates *Il6* transcription. The consensus binding sequence of ATF4 is identical to that of the cAMP response element (CRE) (36). The *Il6* promoter contains an evolutionarily conserved region in which a putative ATF4-binding sequence is located in the vicinity of the NF-κB–binding site (Fig. 5*A*). We, therefore, performed the *Il6* promoter luciferase assay using RAW264 macrophages. The luciferase activity was increased by treatment with LPS, which was further enhanced by ATF4 overexpression (Fig. 5*B*). The effect of ATF4 overexpression was abolished when transfected with the promoter construct containing a mutant CRE. Interestingly, the mutation in the CRE also markedly inhibited the LPS-induced activation of the *Il6* promoter. Consistently, experiments with a series of truncated *Il6* promoter constructs showed marked reduction of the promoter activity in the absence of CRE (Supplementary Fig. 5), suggesting that the CRE is indispensable for the LPS- and ATF4-induced activation of the *Il6* promoter. To confirm the direct recruitment of ATF4 to the *Il6* promoter region, we performed a chromatin immunoprecipitation assay using peritoneal macrophages. Signals from the promoter region containing the CRE were significantly increased upon treatment with palmitate or thapsigargin plus lipid A (Fig. 5*C*). These data suggest that ATF4 directly activates the *Il6* promoter.

DISCUSSION

In this study, we demonstrated that ATF4 is induced downstream of metabolic stresses caused by SFAs and ER stressors. ATF4 exerts its proinflammatory effects through at least two different mechanisms: direct activation of the *Il6* promoter and involvement in NF-κB activation (Fig. 5*D*). According to previous reports, other members of ATF/CREB family of transcription factors are also involved in positive (e.g., XBP1) or negative (e.g., ATF3) regulation of *Il6* expression (18,32). Of note, these factors may be induced downstream of TLR4 stimulation even independent of ER stress (18,32). By contrast, our results suggest that ATF4 is minimally involved in the TLR4 signaling in unstressed cells. Considering that the ATF4 pathway is activated under a variety of metabolic stresses, ATF4 would constitute a critical link between metabolic stresses and *Il6* expression.

Furthermore, our observations that the ATF4 pathway acts in synergy with the TLR4 pathway raise a possibility that metabolic stresses affect innate immune response. Consistent with several previous reports (4–6), our results suggest that TLR4 is required for proinflammatory effects of SFAs. Importantly, the current study also identifies the ATF4 pathway as a novel mechanism of SFA-induced proinflammatory cytokine expression that is induced even in the absence of TLR4. Given that SFAs activate both TLR4 and various metabolic stress pathways upstream of ATF4 (1,4–9), the cross talk between these pathways would be important for better understanding of the molecular mechanism of SFA-induced proinflammatory cytokine expression. Collectively, our findings raise the possibility that ATF4 plays a role in the pathophysiology of chronic inflammation in the metabolic syndrome and type 2 diabetes.

Acknowledgments. The authors thank Dr. Shizuo Akira, Osaka University, for providing *Atf4* haploinsufficient mice; Dr. Toshihiro Ichiki, Kyushu University, for providing *Il6* promoter luciferase plasmids; and Dr. Takahisa Nakamura, Cincinnati Children's Hospital Medical Center, for critical reading of the manuscript.

Funding. This work was supported in part by Grants-in-Aid for Scientific Research from the Ministry of Education, Culture, Sports, Science and Technology of Japan; Japan Science and Technology Agency, Precursory Research for Embryonic Science and Technology; Astellas Foundation for Research on Metabolic Disorders; and Nestlé Nutrition Council, Japan.

Duality of Interest. No potential conflicts of interest relevant to this article were reported.

Author Contributions. Y.I. and T.S. researched data, contributed to the discussion, and wrote, reviewed, and edited the manuscript. R.H., M.K.-S., M.T., and M.H. contributed to the discussion. I.S. researched data and contributed to the discussion. T.T.-I. contributed to network and pathway analyses. M.N. and Y.M. performed the microarray experiments. Y.O. contributed to the discussion and wrote, reviewed, and edited the manuscript. T.S. and Y.O. are the guarantors of this work and, as such, had full access to all the data in the study and take responsibility for the integrity of the data and the accuracy of the data analysis.

References

1. Hotamisligil GS. Endoplasmic reticulum stress and the inflammatory basis of metabolic disease. Cell 2010;140:900–917
2. Odegaard JI, Chawla A. Pleiotropic actions of insulin resistance and inflammation in metabolic homeostasis. Science 2013;339:172–177
3. Osborn O, Olefsky JM. The cellular and signaling networks linking the immune system and metabolism in disease. Nat Med 2012;18:363–374
4. Suganami T, Tanimoto-Koyama K, Nishida J, et al. Role of the Toll-like receptor 4/NF-kappaB pathway in saturated fatty acid-induced

inflammatory changes in the interaction between adipocytes and macrophages. Arterioscler Thromb Vasc Biol 2007;27:84–91

5. Shi H, Kokoeva MV, Inouye K, Tzameli I, Yin H, Flier JS. TLR4 links innate immunity and fatty acid-induced insulin resistance. J Clin Invest 2006;116: 3015–3025
6. Lee JY, Sohn KH, Rhee SH, Hwang D. Saturated fatty acids, but not unsaturated fatty acids, induce the expression of cyclooxygenase-2 mediated through Toll-like receptor 4. J Biol Chem 2001;276:16683–16689
7. Erbay E, Babaev VR, Mayers JR, et al. Reducing endoplasmic reticulum stress through a macrophage lipid chaperone alleviates atherosclerosis. Nat Med 2009;15:1383–1391
8. Holland WL, Bikman BT, Wang LP, et al. Lipid-induced insulin resistance mediated by the proinflammatory receptor TLR4 requires saturated fatty acid-induced ceramide biosynthesis in mice. J Clin Invest 2011;121:1858–1870
9. Nakamura T, Furuhashi M, Li P, et al. Double-stranded RNA-dependent protein kinase links pathogen sensing with stress and metabolic homeostasis. Cell 2010;140:338–348
10. Ozcan U, Yilmaz E, Ozcan L, et al. Chemical chaperones reduce ER stress and restore glucose homeostasis in a mouse model of type 2 diabetes. Science 2006;313:1137–1140
11. Suganami T, Nishida J, Ogawa Y. A paracrine loop between adipocytes and macrophages aggravates inflammatory changes: role of free fatty acids and tumor necrosis factor alpha. Arterioscler Thromb Vasc Biol 2005;25: 2062–2068
12. Ichioka M, Suganami T, Tsuda N, et al. Increased expression of macrophage-inducible C-type lectin in adipose tissue of obese mice and humans. Diabetes 2011;60:819–826
13. Krogan NJ, Cagney G, Yu H, et al. Global landscape of protein complexes in the yeast Saccharomyces cerevisiae. Nature 2006;440:637–643
14. Bergholdt R, Brorsson C, Lage K, Nielsen JH, Brunak S, Pociot F. Expression profiling of human genetic and protein interaction networks in type 1 diabetes. PLoS One 2009;4:e6250
15. Shannon P, Markiel A, Ozier O, et al. Cytoscape: a software environment for integrated models of biomolecular interaction networks. Genome Res 2003;13:2498–2504
16. Dahl JA, Collas P. A rapid micro chromatin immunoprecipitation assay (microChIP). Nat Protoc 2008;3:1032–1045
17. Tian Q, Miyazaki R, Ichiki T, et al. Inhibition of tumor necrosis factor-alpha-induced interleukin-6 expression by telmisartan through cross-talk of peroxisome proliferator-activated receptor-gamma with nuclear factor kappaB and CCAAT/enhancer-binding protein-beta. Hypertension 2009;53: 798–804
18. Suganami T, Yuan X, Shimoda Y, et al. Activating transcription factor 3 constitutes a negative feedback mechanism that attenuates saturated fatty acid/Toll-like receptor 4 signaling and macrophage activation in obese adipose tissue. Circ Res 2009;105:25–32
19. Itoh M, Suganami T, Nakagawa N, et al. Melanocortin 4 receptor-deficient mice as a novel mouse model of nonalcoholic steatohepatitis. Am J Pathol 2011;179:2454–2463
20. Szklarczyk D, Franceschini A, Kuhn M, et al. The STRING database in 2011: functional interaction networks of proteins, globally integrated and scored. Nucleic Acids Res 2011;39(Database issue):D561–D568
21. Joshi-Tope G, Gillespie M, Vastrik I, et al. Reactome: a knowledgebase of biological pathways. Nucleic Acids Res 2005;33(Database issue):D428–D432
22. Harding HP, Zhang Y, Zeng H, et al. An integrated stress response regulates amino acid metabolism and resistance to oxidative stress. Mol Cell 2003;11:619–633
23. Ishiyama J, Taguchi R, Akasaka Y, et al. Unsaturated FAs prevent palmitate-induced LOX-1 induction via inhibition of ER stress in macrophages. J Lipid Res 2011;52:299–307
24. Vattem KM, Wek RC. Reinitiation involving upstream ORFs regulates ATF4 mRNA translation in mammalian cells. Proc Natl Acad Sci USA 2004;101: 11269–11274
25. Ohoka N, Yoshii S, Hattori T, Onozaki K, Hayashi H. TRB3, a novel ER stress-inducible gene, is induced via ATF4-CHOP pathway and is involved in cell death. EMBO J 2005;24:1243–1255
26. Ariyama H, Kono N, Matsuda S, Inoue T, Arai H. Decrease in membrane phospholipid unsaturation induces unfolded protein response. J Biol Chem 2010;285:22027–22035
27. Mason P, Liang B, Li L, et al. SCD1 inhibition causes cancer cell death by depleting mono-unsaturated fatty acids. PLoS One 2012;7:e33823
28. Fu S, Yang L, Li P, et al. Aberrant lipid metabolism disrupts calcium homeostasis causing liver endoplasmic reticulum stress in obesity. Nature 2011;473:528–531
29. Volmer R, van der Ploeg K, Ron D. Membrane lipid saturation activates endoplasmic reticulum unfolded protein response transducers through their transmembrane domains. Proc Natl Acad Sci USA 2013;110:4628–4633
30. Hayden MS, Ghosh S. Shared principles in NF-kappaB signaling. Cell 2008; 132:344–362
31. Tanaka T, Tsujimura T, Takeda K, et al. Targeted disruption of ATF4 discloses its essential role in the formation of eye lens fibres. Genes Cells 1998;3:801–810
32. Martinon F, Chen X, Lee AH, Glimcher LH. TLR activation of the transcription factor XBP1 regulates innate immune responses in macrophages. Nat Immunol 2010;11:411–418
33. Boyce M, Bryant KF, Jousse C, et al. A selective inhibitor of eIF2α dephosphorylation protects cells from ER stress. Science 2005;307:935–939
34. Woo CW, Cui D, Arellano J, et al. Adaptive suppression of the ATF4-CHOP branch of the unfolded protein response by Toll-like receptor signalling. Nat Cell Biol 2009;11:1473–1480
35. Jiang HY, Wek SA, McGrath BC, et al. Phosphorylation of the alpha subunit of eukaryotic initiation factor 2 is required for activation of NF-kappaB in response to diverse cellular stresses. Mol Cell Biol 2003;23:5651–5663
36. Lin YS, Green MR. Interaction of a common cellular transcription factor, ATF, with regulatory elements in both E1a- and cyclic AMP-inducible promoters. Proc Natl Acad Sci USA 1988;85:3396–3400

Signal Transduction

Molecular Cancer Research

ERK-Dependent Downregulation of Skp2 Reduces Myc Activity with HGF, Leading to Inhibition of Cell Proliferation through a Decrease in Id1 Expression

Xiaoran Li[1], Ying Bian[1], Yuri Takizawa[1,2], Tomio Hashimoto[1], Toshiyuki Ikoma[3], Junzo Tanaka[3], Naomi Kitamura[1], Yutaka Inagaki[2], Masayuki Komada[1], and Toshiaki Tanaka[1]

Abstract

Hepatocyte growth factor (HGF) has an inhibitory effect on human HepG2 hepatoma cell proliferation. Previously, it was shown that HGF treatment downregulated Id1 and upregulated $p16^{INK4a}$ in an ERK-dependent manner, leading to the inhibition of cellular proliferation. Here, new insight suggests that Skp2, an SCF complex component and potential prognosticator in cancer, is downregulated by injection of HGF into established HepG2 xenograft tumors. The downregulation was evident at both the mRNA and protein level and in an ERK-dependent manner. Critically, high expression of Skp2 restored HGF-inhibited cell proliferation, indicating that the inhibitory effect of HGF required the downregulation of Skp2. However, downregulation was not involved in the HGF-induced upregulation of a CDK inhibitor, $p27^{Kip1}$, a known SCF-Skp2 target. Instead, data revealed that Skp2 regulated Myc activity, which has oncogenic potential in the generation of hepatocellular carcinoma. Elevated expression of Skp2 or a mutant that is unable to associate with the SCF complex was capable of activating Myc, suggesting that Skp2 does not act on Myc as a component of the SCF complex, and thus functions as an activator of Myc independent of its role in ubiquitination. Furthermore, Skp2 regulated Id1 expression by regulating Myc activity, and the regulation of Skp2 is involved in the activity of p16 promoter through regulation of Id1 expression. Overall, these mechanistic findings provide the first evidence that ERK-dependent downregulation of Skp2 reduced Myc activity, leading to HGF-induced inhibition of cell proliferation through decreased Id1 expression.

Implications: This study elucidates the molecular details of HGF-induced inhibition of cellular proliferation in liver cancer cells. *Mol Cancer Res; 11(11); 1437–47. ©2013 AACR.*

Introduction

Hepatocyte growth factor (HGF) is a pleiotropic glycoprotein produced by stroma cells and associated with heparin in a wide variety of tissues. Its high affinity receptor c-Met is encoded by the c-met protooncogene and is widely expressed in epithelial cells (1). Binding of HGF activates the tyrosine kinase activity of c-Met, leading to cell proliferation, scattering, enhanced motility and so on, and thus HGF plays a key role in tumor–stroma interactions. Aberrant activation of c-Met, which can be induced through its mutation and/or overexpression, causes many kinds of tumors (2). Recent efforts to find substances that inhibit the activation of c-Met are thus expected to lead to suppression of the malignant transformation of cells. However, HGF has an opposing effect on the regulation of cell proliferation in accordance with cell type: it promotes the proliferation of some tumor cells, but suppresses that of others (3, 4). This opposing effect is considered to depend on differences in the downstream pathways of c-Met (3–5). Thus, elucidation of the pathways responsible for the effect is expected to lead to new drugs for the suppression of tumor growth.

The binding of HGF to c-Met induces the phosphorylation of several tyrosine residues on c-Met followed by the recruitment of various signal transducers and adaptors such as Grb2 and Gab1, leading to activation of two major signaling pathways, the extracellular signal-regulated kinase (ERK), and phosphoinositide 3-kinase (PI3K)/Akt pathways (6, 7). We previously showed that HGF treatment of human HepG2 hepatoma cells inhibited cell proliferation by arresting the cell cycle at G_1 (8). This effect was overcome by partial inhibition of the ERK pathway with a low concentration of the MEK inhibitor PD98059, but not by inhibition of the PI3K pathway (7), showing that strong activation of ERK is essential for the inhibitory effect of HGF,

Authors' Affiliations: [1]Department of Biological Sciences, Graduate School of Bioscience and Biotechnology and [2]Department of Regenerative Medicine, Tokai University School of Medicine, Isehara, Japan; [3]Department of Inorganic Materials, Graduate School of Engineering, Tokyo Institute of Technology

Note: Supplementary data for this article are available at Molecular Cancer Research Online (http://mcr.aacrjournals.org/).

Corresponding Author: Toshiaki Tanaka, Department of Biological Sciences, Graduate School of Bioscience and Biotechnology, Tokyo Institute of Technology, 4259 Nagatsuta, Midori-ku, Yokohama, 226-8501, Japan. Phone: 81-45-924-5702; Fax: 81-45-924-5771; E-mail: ttanaka@bio.titech.ac.jp

doi: 10.1158/1541-7786.MCR-12-0718

but activation of the PI3K/Akt pathway is not. The strong activation of ERK by HGF upregulated expression of a Cdk inhibitor, $p16^{Ink4a}$, which led to a redistribution of other Cdk inhibitors, p21 and p27, from Cdk4 to Cdk2, resulting in low phosphorylation of pRb and G_1 arrest (8, 9). Because the upregulation of p16 expression is crucial to the G_1 arrest, we studied the mechanism responsible for it, and found that transcription factor Ets upregulates p16 through downregulation of a repressor protein for Ets, Id1 (10). The expression of Id1 is shown to be regulated at the transcription level (10), but the regulatory mechanism remains to be elucidated.

S-phase kinase–associated protein 2 (Skp2) is an F-box protein in the SCF complex, which consists of Skp1, Cullin, Rbx1 and an F-box protein (11), and is responsible for the ubiquitination and degradation of many kinds of proteins as an E3 ubiquitin ligase. F-box protein functions as the variable substrate-recognition component of the complex. More than 70 F-box proteins are present in the human genome and each is thought to have specific substrates and functions. Thus, the kinds and doses of F-box proteins define the functions of the SCF complex in cellular processes such as the cell cycle, signal transduction, and transcription. The SCF complex including Skp2 (SCF^{Skp2}) regulates G_1–S, the point responsible for defining the progression/arrest of a cell cycle, by regulating the degradation of substrates such as Cdk inhibitors (12). $p27^{Kip1}$, which induces cell-cycle arrest at G_1–S with inhibition of Cdk2/4/6, is a representative Cdk inhibitor suppressed by SCF^{Skp2} (13, 14). Overexpression of Skp2 leads to malignant progression of tumors through acceleration of p27 proteolysis (15, 16), implicating p27 in the function of Skp2 in tumor progression. In contrast, clinical research indicates the absence of an inverse correlation between Skp2 and p27 expression in some human sarcomas (17), suggesting that Skp2 has a p27-independent role in some cancer cells. In fact, a few reports have shown that Skp2 activates the transcription factor Myc through ubiquitination by SCF^{Skp2}, leading to upregulation of target genes involved in cell proliferation such as Cdc2 (18, 19). Also, a recent report showed that Skp2 upregulates expression of the *RhoA* gene, which has a role in cell invasion, by regulating Myc activity independently of the SCF complex (20). Hence, Skp2 seems to function as a regulator in tumorigenesis and cancer progression through various mechanisms.

We previously showed that HGF treatment of HepG2 hepatoma cells leads to suppression of cell proliferation through a redistribution of the Cdk inhibitors p21 and p27. Also, we showed that HGF treatment induces upregulation of p27 expression (9). In this study, we first examined the expression of Skp2, as the amount of p27 may be regulated via protein degradation with SCF^{Skp2}. We found that Skp2 expression is downregulated by injection of HGF into established tumors from HepG2 cells in mice. We conducted a detailed analysis of the role and mechanism of the downregulation with cultured HepG2 cells, and found that the downregulation occurs in an ERK-dependent manner at the mRNA and protein level, but this downregulation is not involved in the upregulation of p27 expression. We then examined the effect of the downregulation on the transcriptional activity of Myc, which has important roles in hepatocarcinoma (21, 22). We found that the downregulation reduces Myc activity, and Skp2 functions as an activator of Myc independently of its role in ubiquitination. Finally, analysis of Id1, which is involved in the regulation of HepG2 cell proliferation, showed that the reduction in Myc activity caused by the Skp2 downregulation decreases Id1 expression, leading to activation of p16 promoter. We revealed in this study that the downregulation of Skp2 expression, which leads to a reduction in Myc activity, is crucial to the inhibitory effect of HGF on the proliferation of HepG2 hepatoma cells. Another hepatoma cell line, HuH7, proliferation of which is suppressed by HGF in an ERK-dependent manner, also showed ERK-dependent downregulation of Skp2 and Id1 suggesting that some cancer cells, other than HepG2 cells, arrest their proliferation by HGF in the same mechanism as HepG2 cells.

Materials and Methods

Cell culture

HepG2 cells and HuH7 cells were provided by Dr. S. Taketani and Dr. N. Kitamura, respectively, and have been described previously (7–10). Cells were cultured as previously described (9).

Reverse transcriptase-PCR

Total RNA was purified with ISOGEN (Nippon Gene) according to the manufacturer's instructions. cDNA synthesis was as described previously (10, 23). PCR was conducted with pairs of specific oligonucleotide primers (Skp2: 5′-CCTGTCTGTGCCTCCCTG-3′ and 5′-CTGAGTGATAGGTGTTGG-3′, $p27^{Kip1}$: 5′-ATGTCAAACGTGCGAGTGTC-3′ and 5′-ACGTTTGACGTCTTCTGAGG-3′). $p16^{Ink4a}$ and GADPH were amplified with primers as described previously (9). PCR products were resolved on a 1.5% agarose gel and visualized with ethidium bromide staining.

Antibodies and immunoblotting

Detailed antibodies were described in Supplementary Data. Cell lysates were prepared as described previously (10). Equal amounts of protein in the precleared cell lysates (20–70 μg total protein) were resolved by SDS-PAGE on a 12% gel after heat denaturation. Immunoblotting was conducted as described previously (9, 24).

Established tumors originating from HepG2 cells

Nonobese diabetic/severe combined immunodeficiency (NOD/SCID) mice were purchased from Oriental Yeast Co., Ltd. Animal experiments were carried out in accordance with the institutional guidelines of Tokai University (Isehara, Japan). To deplete NK cells in the mice, 200 μL of 1 mg/mL anti-asialo GM1 antiserum (Wako Pure Chemical Industries, Ltd) was administered every 4 days. The mice were inoculated subcutaneously with 5×10^6 HepG2 cells into the dorsal flanks. After establishment of tumors, HGF or PBS in a total volume of 200 μL was injected directly into the tumor tissues (100–130 mm^3) for 7 consecutive days.